State of Charge and Capacity Tracking in VRFB Systems

by

Kalvin Schofield

A thesis submitted in partial fulfillment of the requirements for the degree of

Master of Science

in

Energy Systems

Department of Electrical and Computer Engineering
University of Alberta

© Kalvin Schofield, 2022

Abstract

Numerous battery technologies have been developed, each with their own advantages and disadvantages which are discussed herein. An emerging form is the vanadium redox flow battery (VRFB), which utilizes vanadium's two soluble redox couples to create a fully liquid state system based off a single metal. The VRFB electrolyte is prone to several degradation mechanisms which reduces its capacity over time. While state of charge (SOC) monitoring is commonly done via voltage, this is only able to detect symmetrical capacity losses across the full system. As the electrolyte displays brilliant color changes upon cycling, the SOC may be monitored via electrolyte absorbance. As the proposed method is able to monitor each electrolyte individually, asymmetrical capacity losses may be detected. The primary goal of this thesis is to a) develop a flow cell which allows for optical monitoring of a continuous flow of acidic electrolyte, b) develop a measurement system capable of monitoring an electrolyte's absorbance of a white light source, and c) determine the suitability and accuracy of this technique for SOC monitoring of the VRFB anolyte and catholyte. Testing is performed on a 2.5 kW, 40 cell VRFB stack with 8L and 40 L volumes of electrolyte. An automatic electrolyte re-balancing mechanism is constructed by adding a hydraulic shunt between the two tanks, which has successfully demonstrated the ability to recover symmetric capacity loss due to net water transport. For continual monitoring of asymmetric losses, an FD11a photodiode was used to monitor electrolyte absorbance in a custom-made flow cell with thicknesses of 1/4", 1/8", 1/16". Although experiments were unsuccessful due to the high absorbance of the electrolyte, results displayed promise should a smaller optical path/stronger light source be used.

Acknowledgements

A special thank you to Dr. Musilek for his support in making this project become a reality. Additional thanks to Peter, Carolina, and Nazli for your invaluable help with the VRFB system and experiments. Thank you to my family for putting up with me for these long years.

Table of Contents

List of Tables

List of Figures

Chapter 1

Introduction

Traditionally, the main source of electricity production has been through the burning of fossil fuels. This process typically produces large amounts of greenhouse gasses which are detrimental to the environment [1]. In recent years, electricity production has been shifting towards renewable energy sources which commonly have a smaller ecological footprint. Among these are wind and solar, additions of which have generally taken a priority [2]. Contributions from these sources are expected to account for 20% of the EU's gross energy consumption in 2020 and grow to 60% by 2050 [3].

Canada currently procures most of its renewable energy from moving water, although wind and solar utilization have been following an upward trend in the past 10 years [4]. This trend is expected to continue in the future, with Alberta planning to phase out its coal generation (which accounted for 48% of total energy production 2016) and add 5000 MW of energy production from renewable sources [5]. The transition has contributed to the steady reduction of Canada's greenhouse gas emissions observed since 2003 [6].

Although economically and environmentally appealing, these sources are prone to intermittency. Possibly manifesting as capacity mismatches, this has a negative impact on grid performance and reliability, which must be maintained to avoid equipment damage or blackouts. This problem is becoming ever more relevant with further renewable energy additions and the electric vehicle market expected to boom in com-

ing years [7, 8].

One approach to mitigate these issues is the integration of energy storage devices, such as batteries, into the grid. These devices may be charged when additional energy is available, and supply energy at times of high demand or when energy supply via renewable sources is low. They may also be used for economic dispatch or power quality management applications. For these and other related applications, a state of charge (SOC) monitoring system is required. These measurements allow users to track the energy at every node in their system, and use it optimally based on system conditions. It also allows the user to avoid equipment damage which may occur do to overcharging or undercharging the battery.

1.1 Motivation

Vanadium redox flow batteries (VRFBs) are an emerging battery technology with many attractive properties. Vanadium's four oxidation states are soluble in aqueous environments, allowing all active materials to be stored and utilized in liquid form. The chemical similarities between the anolyte and catholyte limits cross-contamination of the electrolytes while avoiding degradation caused by solid-state reactions. This reduces capacity fade, allows for a high cycle life, and cuts down on the amount of battery maintenance required. The electrolyte solutions are pumped through an electrochemical cell, kept separate in two half-cells by means of an ion exchange membrane [9, 10]. Energy can then be stored or generated through redox (reduction-oxidation) reactions occurring in the cell, cycling the vanadium ions through their available oxidation states (the V^{5+}/V^{2+} redox pair is converted to V^{4+}/V^{3+} during discharge) while charge balance is preserved via ion transport through the cell membrane.

The water weight of these batteries results in a poor energy density and limits them to stationary applications. However, they are still very appealing due to their high cycle life, high round-trip energy efficiency, and are not susceptible to undercharging.

They are also versatile in many applications as the power and capacity of these systems can be scaled independently.

Capacity losses may arise from mechanisms such as imbalanced vanadium-ion transfer or water transport across the membrane, which may be counteracted through periodic remixing of the anolyte and catholyte [11]. However, unequal degradation mechanisms may occur between the tanks (*e.g.* air oxidation of V^{2+}, oxygen and hydrogen evolution, precipitation of V^{5+} as V_2O_5) [12]. These mechanisms result in the reduced capacity of one electrolyte, and chemical or electrochemical must be used to regenerate the electrolyte [13]. Therefore knowing the oxidation state present in each tank can be beneficial for optimal rebalancing. Methods such as open-circuit voltage (OCV) monitoring can be done to monitor the total system SOC as modelled by the Nernst equation. However, this method is is only able to detect symmetrical capacity losses in the system. Additionally, the onset of asymmetrical electrolyte imbalances causes the measured OCV to change such that the Nernst equation no longer accurately depict the SOC.

An optimal SOC monitoring technique would have the ability to monitor each individual electrolyte to calculate individual SOC values for each half-cell. One method of achieving this is potentiometric titration (typically with a potassium permanganate titrant), but the time requirement makes it unsuitable for real-time applications [10]. Individual voltage measurements could be done by inserting inert electrodes into each electrolyte reservoir, but is impractical due to drift in the measured potential [13]. Conductivity measurements on each electrolyte can be done, but requires probe calibration for accurate measurements [13], and is sensitive to temperature. A four-pole device in each half-cell electrolyte could be used to measure the voltage drop when passing constant current through the outer poles [10]. Although it eliminates the polarization effect and the measured voltage directly arises from the electrolyte characteristics, it is sensitive to the apllied current (poor voltage sensitivity when low, inaccurate measurements when high). Due to each oxidation state having its own

unique color, color changes may be observed and tracked during battery cycling [13, 14]. This allows for relatively simple SOC monitoring via absorbance of light, and electrolyte health to be independently monitored for each half-cell.

Although still having some temperature dependence, the main challenge of this method is the high absorbance of the electrolyte, specifically the positive electrolyte. This can be overcome by using a stronger light source or a thinner layer of electrolyte. Previous scientific research has typically been done with spectrophotometers to developed SOC vs absorbance relationships over a range of SOC values. For commercial or field applications, a simpler (and possibly much cheaper) system could be developed to measure the bulk absorbance of a white light source. Measuring the absorbance through a clear flow-through type cuvette allows for measurements to be taken continuously and in-situ.

1.2 Thesis Objectives

The goal of this thesis is to develop an absorbance-based sensor able to determine individual SOC values for the positive and negative electrolytes of a VRFB continuously and in-situ.

Deliverables

1) Electrolyte Visualization: As the VRFB electrolyte is very dark, absorbance testing must be done on a thin layer of electrolyte. A flow cell was developed for this purpose, which allows for optical monitoring of a continuous flow of acidic electrolyte. Previous studies on VRFB electrolytes have shown success with wavelengths in the UV-vis spectrum, and as such material selection was done to ensure adequate transmission of these wavelengths. Clear acrylic sheets are used as endplates, with mechanical stability and water-tightness being provided by eight $\frac{1}{4}$" bolts. The sandwich-type structure allows for easy alteration of the cell's internal cavity, and hence the optical path through the electrolyte. To reduce measurement errors, attempts were made to minimize the amount of ambient light passing through the cell.

2) Electronics: A simple photodiode circuit was created to monitor the transmittance of a white light source through the flow cell/electrolyte. The main components of the circuit are the photodiode, a load resistor for conversion of the photodiode current into a voltage, and a noise filter (capacitor and resistor) under a reverse bias of 24 V. These components are milled onto a 1.5 mm thick copper clad PCB.

3) Characterization/accuracy: Experiments were performed to assess the success, suitability, and accuracy of this technique for SOC detection in a VRFB system. The photodiode voltage is analyzed and compared with the stack voltage/current/time data during cycling of a 2.5 kW, 40 cell VRFB stack to allow a relationship to be formed between the electrolyte absorbance and SOC.

1.3 Thesis Outline

Background information is contained in chapter 2, beginning with a summary of common battery types (lead-acid, lithium-ion, sodium-sulfur and vanadium-redox flow batteries) in section 2.1. Common SOC measurement techniques for these systems are discussed in section 2.2, while a more detailed discussion on SOC measurement via light transmission is discussed in section 3.

Details about the experimental setup are found in Chapter 4. The design and instrumentation of the VRFB setup is discussed in section 4.1, followed by details regarding construction of the SOC detection system found in section 4.2. The cost of these systems are outlined within section 4.3. Experimental procedures are discussed in section 4.4, the results of which are discussed in chapter 5.

Initial experiments were performed utilizing a small volume of electrolyte (section 5.1). Future experiments were performed with a larger volume of electrolyte (section 5.2). To assess the effect of charging current on battery performance, initial cycling tests were performed at 15 A (section 5.2.1), before being increased to 30 A (section 5.2.2). Similarly, the effect of discharging current was assessed in section 5.2.3, with the maximum current being increased from 5.5 A to 45 A. As an secondary cell

was not used to measure the systems OCV (cell voltage at zero applied current), continuous observation of the OCV during charge/discharge process is not possible. However, discharging the stack in small segments (with a small amount of relaxation time between each segment) allows OCV-SOC experiments to be performed in order to observe the relationship between terminal and open-circuit voltages. Results from these experiments are found in section 5.2.4. Based on the results of all previously mentioned experiments, section 5.2.5 provides a summary of the success/failure of each design change, and suggestions for successful VRFB operation during future experiments.

Results from the SOC sensor are found in section 5.3, with results from the negative and positive electrolyte being found in sections 5.3.1 and 5.3.2 respectively. These results are summarized in section 5.3.3 with a discussion of this technique's suitability for continuous SOC monitoring in a VRFB system.

Chapter 2

Background

2.1 Energy Storage Technologies

Numerous types of battery energy storage technologies are available. Each of them possesses its own advantages/disadvantages arising from the system's chemical characteristics. This section investigates common battery types in terms of their chemical operation and their benefits in various applications.

2.1.1 Lead-Acid Batteries

Lead-acid batteries are among the most mature and widely used battery types. These batteries consist of $PbO_{2(s)}$ and $Pb_{(s)}$ electrodes immersed in sulfuric acid. During discharging, these electrodes react with the sulfuric acid, forming $PbSO_{4(s)}$ at both electrodes. These are shown in equations 2.1 and 2.2, with the resultant full-cell reaction being given by equation 2.3.

$$PbO_{2(s)} + HSO^{-}_{4(aq)} + 3H^{+}_{(aq)} + 2e^{-} \rightarrow PbSO_{4(s)} + 2H_2O_{(l)} \tag{2.1}$$

$$Pb_{(s)} + HSO^{-}_{4(aq)} \rightarrow PbSO_{4(s)} + H^{+}_{(aq)} + 2e^{-} \tag{2.2}$$

$$PbO_{2(s)} + Pb_{(s)} + 2H_2SO_{4(aq)} \rightarrow 2PbSO_{4(s)} + 2H_2O_{(l)}, E^0 = 2.05V \tag{2.3}$$

The electrodes are separated by a microporous layer such as polyvinyl chloride (PVC) or rubber in the case of a flooded lead-acid battery. The main requirements of

this separator are a) high porosity to preserve the ionic conductivity (via sulfuric acid uptake), b) high tortuosity to limit lead penetration through the membrane. Sulfuric acid is produced/consumed during cycling, creating density and concentration gradients which may affect the active material usage and tendency for sulfation. This is limited in the case of sealed cells, which are typically created by immobilizing the electrolyte in an absorptive glass mat (AGM) or silica gel [15, 16].

These batteries are highly reliable, have a low cost (300-600 $\$/kW$), have strong surge capabilities, and have a high efficiency [17]. However due to water weight, their energy density is limited to 50 Wh/kg, and they have poor low temperature performance [17, 18].

Oxygen evolution may occur at the positive electrode (equation 2.4), while hydrogen evolution may occur at the positive electrode (equation 2.5). This results in water loss, which contributes to their short lifetime of 1000 cycles, after which replacement or refurbishment is required [17, 18]. This can be mitigated via charge voltage control, and by adding water occasionally in the case of unsealed batteries [15].

$$H_2O_{(l)} \rightarrow \frac{1}{2}O_{2(g)} + 2H^+_{(aq)} + 2e^- \tag{2.4}$$

$$2H^+_{(aq)} + 2e^- \rightarrow H_{2(g)} \tag{2.5}$$

This is limited in the case of sealed batteries, as oxygen may travel (through a network of empty AGM pores) to the negative electrode and recombination can occur as per equation 2.6 then converted to lead as per the normal charge process [15]. Another mechanism is the electrochemical reaction of oxygen on the electrode surface (reverse reaction of equation 2.4) [19]. However, water loss may still occur, especially in the case of high charge voltages or due to hydrogen evolution, causing capacity loss and eventual failure as the cell dries out.

$$Pb_{(s)} + \frac{1}{2}O_{2(g)} + H_2SO_{4(aq)} \rightarrow PbSO_{4(s)} + H_2O_{(l)} \tag{2.6}$$

Lead-acid batteries also have poor deep discharge resistance which reduces their lifetime upon doing so. One study showed that the positive electrode can lose 50% of its capacity over 30 deep discharge cycles, likely due to the formation of insulative barriers (ex $PbSO_4$ and $\alpha - PbO$) [20].

2.1.2 Lithium-Ion Batteries

Lithium-ion batteries have many attractive properties including their high efficiencies ($> 95\%$) and long cycle life (3000 cycles at 80% depth of discharge) [17]. They also have high energy density (200 Wh/kg) and power density [17], owed to the fact that lithium has the lowest atomic weight and highest negative potential compared to other metals [16]. This allows them to be lightweight and have made them an attractive option for portable electronics and electric vehicle applications.

The main hindrances of this battery type are it's high cost and circuitry needed for protection, as lithium metal on its own is highly reactive with air and most liquid electrolytes [16, 17, 21]. Furthermore, electrical shorts may be caused by stress events such as charging below freezing, deep discharging, and excessive vibration or heat. Small shorts act to increase the self-discharge rate, while larger shorts may lead to thermal runaway (overheating and possible fire) [21].

However, the lithium in modern cells is chemically bound such that it cannot easily react, and the cells are designed such that there is no free lithium present at any stage of the cycling process [22]. A polyanion such as $LiFeO_4$ could be used for the cathode, but it is more commonly a layered metal oxide (typically cobalt (expensive, technically preferable), nickel, or manganese(cheapest)) such as lithium-doped cobalt oxide Li_xCoO_2; graphitic carbon is typically used as the anode [16, 23]. During discharge, lithium ions are released from the anode, travel through the electrolyte,

and are embedded in the cathode. This process is illustrated by equations 2.7 and 2.8, with the resultant full-cell reaction being given by equation 2.9.

$$CoO_{2(s)} + Li^{+}_{(aq)} + e^{-} \rightarrow LiCoO_{2(s)} \tag{2.7}$$

$$LiC_{6(s)} \rightarrow C_{6(s)} + Li^{+}_{(aq)} + e^{-} \tag{2.8}$$

$$LiC_{6(s)} + CoO_{2(s)} \rightarrow C_{6(s)} + LiCoO_{2(s)} \tag{2.9}$$

Organic electrolytes are typically used as they are stable against the reduction of lithium and gassing reactions caused by the high cell voltage (4.1 V OCV at full charge) [16]. Although this is the case, overcharging should still be avoided to preserve battery lifetime and performance. If overcharged, the positive electrode becomes supersaturated with lithium, producing lithium oxide (equation 2.10). Further overcharging results in the formation of cobalt (IV) oxide (equation 2.11). These electrode degradation mechanisms must be avoided, typically through proper voltage monitoring/control.

$$Li^{+}_{(aq)} + e^{-} + LiCoO_{2(s)} \rightarrow Li_2O_{(s)} + CoO_{(s)} \tag{2.10}$$

$$LiCoO_{2(s)} \rightarrow CoO_{2(s)} + Li^{+}_{(aq)} + e^{-} \tag{2.11}$$

2.1.3 Sodium-Sulfur Batteries

Sodium-sulphur batteries (NaS) can be cycled up to 4500 times at high efficiency (75-90%) and power density (150-240 Wh/kg) [17]. They also have one of the fastest response times with a 1 ms startup speed [22]. Another appealing feature is their environmental friendliness. Their sealed design eliminates emissions, and 99% of their weight can be recycled [24].

These batteries utilize molten sodium (held in a chamber) as the anode and molten sulfur as the anode, and as such must be kept between 300-350 °C [17, 24–26]. This contributes to their relatively high cost ($2000/kW or $350/kWh), and also poses safety hazards preventing their widespread adoption. Some attempts have been made to create room temperature NaS batteries, but they tend to suffer from low capacity and cycling problems due to a poor electrode/electrolyte compatibility [25]. Nevertheless, some studies have found that they are the most economical battery option for energy management in distribution networks [27].

During discharge, the molten sodium is oxidized to Na^+ (equation 2.12), travels through the solid electrolyte until it reaches the molten sulfur cathode (reduced to S^{2-} as per equation 2.13). Here, sodium and sulfur react to form a sodium polysulfide melt (equation 2.14). The internal resistance is dominated by the electrolyte/separator, a $\beta - Al_2O_3$ ceramic, and is the main factor determining cell performance [24]. The electrolyte structure consists of tightly packed spinel blocks providing mechanical strength and loosely packed conduction slabs which rapidly conduct sodium ions. The ratio of these structures can be changed by altering the electrolyte's sodium/aluminum ratio, allowing conductivity and strength to be optimized based on the system design [24, 28].

$$2Na_{(l)} \rightarrow 2Na^+_{(l)} + 2e^- \tag{2.12}$$

$$xS_{(l)} + 2e^- \rightarrow S^{2-}_{x(l)} \tag{2.13}$$

$$2Na_{(l)} + xS_{(l)} \rightarrow Na_2S_{x(l)} \tag{2.14}$$

At first sight one would assume that the reaction proceeds such that x=1. However, phase diagrams show that an operating temperature of 900 °C would be required to avoid precipitation of Na_2S_2 [26, 28, 29]. As such the reaction is typically halted

after reaching a composition of Na_2S_3 [26]. The composition also has a large effect on the cell voltage, as it passes through single-phase and two-phase regimes over its SOC range. For melts with $>$ 78 wt% sulfur, two immiscible liquids are present (sulfur and $Na_2S_{5.2}$) resulting in a constant 2.076 V. A single polysulfide melt Na_2S_X phase exists at approximately 60% depth of discharge, after which the voltage drops linearly with composition until reaching 1.74 V (corresponding to $Na_2S_2.7$). Na_2S_2 precipitation occurs beyond this point, but the cell voltage remains constant at 1.74 V, as the composition and activity of the liquid phase remains fixed [26, 28].

2.1.4 Vanadium Redox Flow Batteries

A VRFB utilizes four oxidation states of vanadium, typically dissolved in a sulfuric acid solution. A stabilization agent such as HCl or H_3PO_4 can be used to improve the vanadium ion solubility and hence the electrolyte's energy density. The electrolyte is stored in two tanks and pumped through an electrochemical stack where reduction-oxidation reactions occur at the graphite electrodes. The positive electrolyte is charged from the V^{4+} to the V^{5+} state (equation 2.15), while the negative electrolyte is charged from the V^{3+} to the V^{2+} state (equation 2.16) and two protons are generated for every V^{5+} produced in the positive half-cell. Charge conservation is preserved via H^+ or SO_4^{2-} crossover through an ion-selective membrane separating the two tanks.

$$VO^{2+}_{(aq)} + H_2O_{(l)} \rightarrow VO^{+}_{2(aq)} + 2H^{+}_{(aq)} + e^-, E^0 = 1.0V \tag{2.15}$$

$$V^{3+}_{(aq)} + e^- \rightarrow V^{2+}_{(aq)}, E^0 = -0.26V \tag{2.16}$$

$$VO^{2+}_{(aq)} + H_20_{(l)} + V^{3+}_{(aq)} \rightarrow VO^{+}_{2(aq)} + 2H^{+}_{(aq)} + V^{2+}_{(aq)}, E^0 = 1.26V \tag{2.17}$$

Some suppliers form a $V^{3.5+}_{(aq)}$ solution prepared with equimolar amounts of $V^{3+}_{(aq)}$ and $V^{4+}_{(aq)}$, such as the 1.6 M $V^{3.5+}_{(aq)}$ solution produced by Oxkem [30]. In this case,

a pre-charge step occurs in each electrolyte tank prior to regular cycling in order to generate a single oxidation state in each tank. Equation 2.18 occurs in the negative tank while the inverse occurs in the positive tank. This results in a $V^{3+}_{(aq)}$ - $V^{4+}_{(aq)}$ redox couple between the tanks, commonly associated with 0% SOC.

$$VO^{2+}_{(aq)} + 2H^{+}_{(aq)} + e^{-} \rightarrow V^{3+}_{(aq)} + H_2O_{(l)}, E^0 = 0.34V \tag{2.18}$$

The lack of solid state reactions and cross-contamination drastically improves the lifetime and reduces the maintenance of VRFBs. Due to their low energy density, they are limited to stationary applications such as backup power supply or telecommunication applications. They can be tailored to each individual applications requirements via independent scaling of capacity and power ratings.

Although the lack of solid-state reactions drastically improves the VRFB's cycle life, electrolyte degradation can occur still occur. One of these mechanisms is via ion crossover through the membrane. After doing so, the ions quickly reach an equilibrium with their surroundings such that a maximum of two oxidation states are present in each half-cell, which can be described with equations 2.19, 2.20 and 2.21 [31, 32].

$$V^{2+}_{(aq)} + VO^{2+}_{(aq)} + 2H^{+}_{(aq)} \rightarrow V^{3+}_{(aq)} + H_2O_{(l)} \tag{2.19}$$

$$V^{2+}_{(aq)} + VO^{+}_{2(aq)} + 2H^{+}_{(aq)} \rightarrow V^{3+}_{(aq)} + VO^{2+}_{(aq)} + H_2O_{(l)} \tag{2.20}$$

$$V^{3+}_{(aq)} + VO^{+}_{2(aq)} + 2H^{+}_{(aq)} \rightarrow 2VO^{2+}_{(aq)} + H_2O_{(l)} \tag{2.21}$$

This self-discharge process is undesirable due to the reduction of coulombic efficiency and increase in charging time. Additionally, the membrane is selective and ion permeability through it is different for each oxidation state. This leads to a net ion and water content transfer in one direction, reducing capacity and performance over

repeated cycling. This may be detected by techniques such as OCV monitoring, and mitigated by periodic remixing of the electrolytes due to its symmetric nature.

However, many of the VRFB degradation mechanisms are asymmetric and affect the electrolyte solutions differently (for example: $V^{2+}_{(aq)}$ oxidation via oxygen at the negative electrode, $V^{3+}_{(aq)}$ reduction after hydrogen evolution at the negative electrode, $VO^{+}_{2(aq)}$ precipitation as $V_2O_{5(s)}$ at the positive electrode) [12]. Dominance of a particular mechanism may cause the system to become imbalanced (equation 2.22 no longer holds true), and battery performance is dominated by the reduced capacity of one of the electrolyte reservoirs. This is extremely relevant for long term usage as it cannot be mitigated by periodic remixing of the electrolytes, and the electrolytes must be regenerated via a chemical or electrochemical technique.

To monitor the onset of these imbalances, the SOC measurement system should be able to calculate the individual SOCs/oxidation states for each electrolyte, as full-system measurements such as open-circuit voltage (one of the most common SOC measurement techniques) are unable to accurately determine the full extent of these imbalances (knowledge of which would be required in order to apply a suitable regeneration technique). Protons are generated in the positive chamber during charging (equation 2.15), half of which are transferred across the membrane to preserve charge balance. This will increase the conductivity of both half-cell electrolytes, the continuous monitoring of which can be correlated to half-cell SOC or oxidation states [13]. Another method is to monitor color changes in the electrolyte, as each oxidation state possess' its own distinct color. Upon charging, the negative electrolyte transitions from green to violet while positive electrolyte transitions from blue to yellow. By tracking the absorbance changes of an incident light source through the electrolyte with a CCD or photodiode, the SOC of each electrolyte can be determined [12–14]. These methods are discussed in more detail in section 2.2.

2.2 SOC Measurement Techniques

There are a number of SOC measurement techniques which could be utilized for long-term battery monitoring. As the electrolyte is generally one of the most expensive components of a VRFB system, an ideal system should be capable of utilizing atleast one of these techniques to monitor electrolyte health and employ regeneration mechanisms in order to mitigate performance losses and extend the electrolyte lifetime. However, due to the fact that a VRFB is comprised of two aqueous electrolytes which are pumped through a stack continuously, and as such there are many challenges that must be overcome to develop a suitable in-situ monitoring technique. This section outlines some of the most common and promising techniques which aim to overcome these challenges and perform long-term SOC monitoring of a VRFB.

2.2.1 Open-circuit voltage

Open-circuit voltage (OCV) is one of the most commonly used techniques to measure a battery's SOC. In the case of a VRFB using identical quantities of electrochemically available vanadium ions in each half-cell/electrolyte tank, SOC can be expressed as equation 2.22 [12]. Due to the increasingly large difference in the oxidation states between the tanks (V^{3+}/V^{4+} vs V^{2+}/V^{5+}), an increase in the open-circuit voltage (OCV) can be observed while charging. Using the Nernst equation and the assumptions present in equation 2.22, OCV can be modelled and predicted via equation 2.23 during battery cycling [12].

$$SOC = \frac{[V^{2+}_{(aq)}]}{[V^{2+}_{(aq)}] + [V^{3+}_{(aq)}]} = \frac{[VO^{2+}_{(aq)}]}{[VO^{2+}_{(aq)}] + [VO^{+}_{2(aq)}]} \tag{2.22}$$

$$E = E^0 + \frac{RT}{F} ln(\frac{SOC^2([H^+] + SOC)^2}{(1 - SOC)^2}) \tag{2.23}$$

where $[i]$ is the concentration of element i, E^0 is the standard potential (1.26 V), R is the universal gas constant, T is the temperature in degrees K, and F is Faraday's

constant. These OCV measurements are typically done using a separate single-cell operating at zero current, which is typically low cost in relation to other system components. The simplicity, non-intrusiveness, and compact nature of this approach has assisted its rise to become one of the most commonly utilized techniques for SOC measurement.

However, as discussed in section 2.1.4, imbalances may arise due to preferential ion transfer or dominant degradation mechanisms in the positive or negative electrolyte. In this case, equation 2.22 no longer holds true, and the measured potential is no longer governed by equation 2.23. This leads to inaccuracies in the estimation of SOC, the extent of which is not able to be determined using this approach. This is illustrated in Figure 2.1 for the case of V^{5+} precipitation and preferential ion transfer into the positive electrolyte, assuming no re-calibration is done to account for reduced capacity.

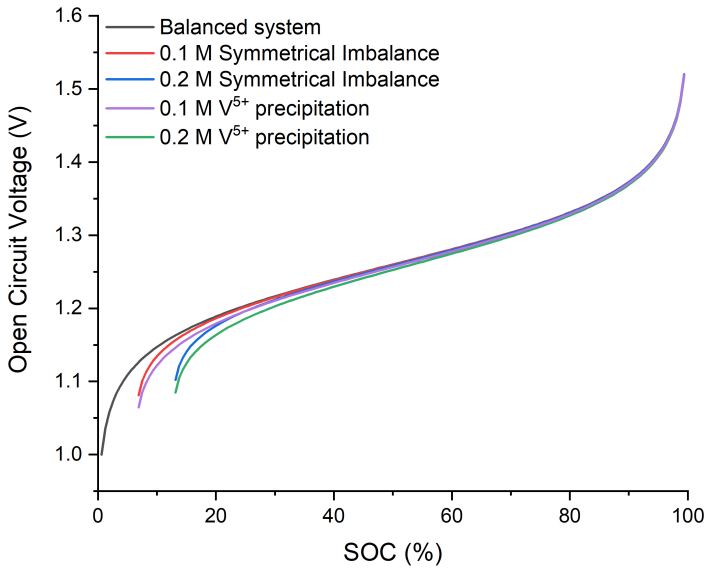

Figure 2.1: Open circuit voltage measurement deviation from the Nernst equation due to symmetrical (ion transfer from anolyte to catholyte) and asymmetrical (V^{5+} precipitation) imbalances in a 1.6 M electrolyte

Capacity loss due to preferential ion transfer may be mitigated via remixing of

the anolyte and catholyte, rebalancing the ion concentration in each tank. However, due to the asymmetrical nature of the V^{5+} precipitation, remixing of the electrolytes will not result in a complete recovery of electrolyte capacity. To fully rebalance the oxidation states in the case of V^{5+} precipitation, V^{2+} oxidation etc, the oxidation states in each tank must be known. But as is seen in Figure 2.1, OCV measurements are unable to achieve this, nor determine whether capacity loss is being caused by a symmetric or asymmetric process.

Theoretically, individual voltage measurements could be done by inserting inert electrodes into each electrolyte reservoir. However, utilizing this method requires a stable reference electrode potential, and would be impractical in large scale systems due to the number of interferences which may lead to drift in the measured potential [13]. In addition, this method has poor sensitivity in calculating SOC, as the potential only changes slightly over a wide SOC range.

2.2.2 Conductivity

It can be noted from equation 2.23 that the magnitude of voltage change during battery cycling is dependant on the proton concentration ($[H^+]$) in the electrolyte. Protons are generated in the positive chamber during charging (equation 2.15), half of which are transferred across the membrane to preserve charge balance. This process leads to an observable conductivity increase in both half-cell electrolytes, and as such, continuous conductivity measurements may be performed independently and correlated to each half-cell's SOC or oxidation states [13].

Previous studies have successfully used conductivity probes to measure each half-cell's SOC, although with relatively low sensitivity [13]. Improvements on this technique include the development of a four-pole device, where a current is passed through the outer poles, and the voltage drop through the electrolyte is measured via the inner poles [10]. Although this method allows for the reduction of polarization errors, it is prone to the current applied by the outer poles (a low current results in poor voltage

sensitivity, while inaccuracies are introduced at high currents).

The electrolyte's conductivity will also be influenced by electrolyte's initial concentration of protons (as most typical VRFB electrolytes utilize an acidic base such as hydrochloric acid or sulfuric acid [33]). Because of this, calibration needs to be performed for each specific electrolyte chemistry or supplier. In addition, measurement errors may be introduced due to this method's temperature dependence or drift in the reference electrode potential. As such, extensive calibration may be required both before and periodically during battery operation.

2.2.3 Optical Techniques

The color of the VRFB electrolyte is dependant on the oxidation state/states of vanadium are present. As such, distinct, observable color changes occur during battery cycling. During charging, the positive electrolyte can be seen transitioning from blue $\rightarrow$ yellow (corresponding to a change from V^{4+} to V^{5+}), while the negative electrolyte can be seen transitioning from green $\rightarrow$ violet (corresponding to a change from V^{3+} to V^{2+}). Due to these color changes, there will be a change in the electrolyte's absorbance of light, which can be correlated with SOC.

One of the most basic components required for this technique is a light source capable of generating wavelengths in the area of interest. Some studies have been done using this approach in an attempt to measure SOC based on its light absorbance. Typical scientific studies utilize a spectrophotometer in order to generate and measure the electrolyte's absorbance of different wavelengths in the UV-Vis range [12–14]. Such systems generally use a spectrometer-type detector (such as a diffraction grating and CCD), in order to detect the wavelength-dependent transmission of light through the sample.

In these cases, the electrolyte is typically studied while contained in a quartz cuvette. While other cheaper materials may be used, such as optical glass, quartz is typically used due to its low absorbance in the UV region (which is typically utilized

in such studies) [34]. While most conventional cuvettes are simply a small (ex 0.05 mm) cylinder to contain a small static amount of electrolyte, a flow-through type cuvette can allow for continuous measurements in-situ.

Theoretically, 'bulk' absorbance measurements could be done using a multi-wavelength light source (ex a white light source) [13]. Doing so would allow for a cheaper measurement system to be created. Firstly, the light source may be cheaper as it no longer needs to be capable of generating UV wavelengths. As such, the sample cuvette may be made using cheaper materials such as optical glass, since low absorbance of UV wavelengths is no longer required. Meanwhile, a simple photodiode may be used to calculate absorbance, and no diffraction gratings or CCDs are required (as the absorbance of a specific wavelength is no longer being measured).

One drawback of this bulk-wavelength absorption method is the non-linearity that is introduced into the data. For example, when performing single-wavelength measurements on the negative electrolyte, linear absorbance/SOC relationships can be observed for certain wavelengths (ex 750 nm [13], 410 nm [14]). However, a parabolic relationship can be seen when using 'bulk' wavelengths in the 300-850 nm range [13]. This challenges is also present for the positive electrolyte, which has a much higher absorbance and displays a parabolic relationship even when using single wavelengths (ex 575 nm, 754 nm).

The high absorbance places constraints on the experimental setup of the system (small optical paths through the electrolyte are required), and complicates data analysis due to the non-linear relationships between absorbance and SOC (especially in terms of the positive electrolyte). The application of a sufficiently thin cuvette may assist in overcoming the high absorbance constraints. While the use of a white light source simplifies the measurement procedures and required data analysis, sensitivity may be reduced in comparison to single-wavelength measurements. However, the reduced cost and simplicity of this method makes it a promising contender for larger-scale systems contingent on future research and classification.

Chapter 3

SOC Measurement via Light Transmission

Spectrophotometry provides quantitative measurements of a material's reflective and transmissive properties as a function of wavelength [35]. Light, most commonly in the UV and visible regions of the spectrum, is produced from a light source and typically focused using a collimating lens. A monochromator such as a diffraction grating or prism can be used to split the light into wavelength bands travelling in different directions. A slit can then be used to allow specified wavelengths to pass through a cuvette containing the sample of interest. The transmitted light is then detected, typically by a photodiode or charge-coupled device (CCD), amplified, and converted to a digital reading such as absorbance, transmittance, concentration, or state of charge (after calibration). This basic structure can be seen in Figure 3.1.

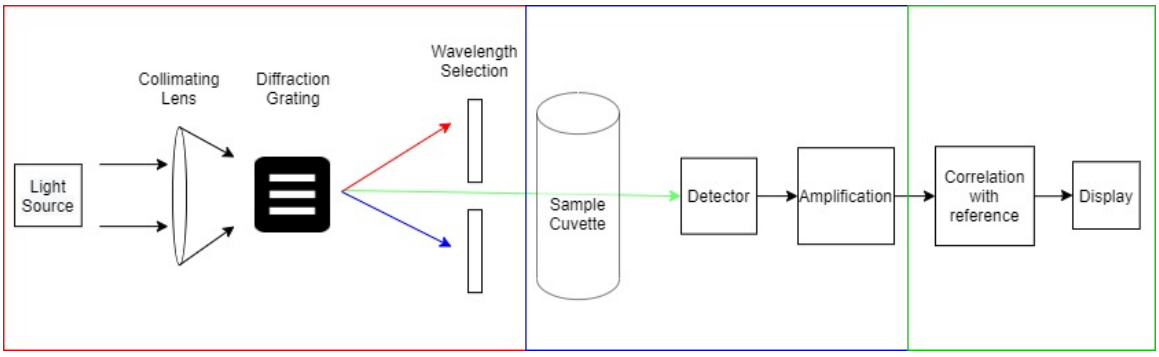

Figure 3.1: Basic structure of a spectrophotometry system. Includes 1) light generation and wavelength selection (red box), 2) detection of transmitted photons (blue box), and 3) data conversion from analog to digital (green box)

3.1 Light Generation

Common light source choices include deuterium arc lamps for the UV range (190-400 nm), light emitting diodes (LEDs) for the visible region, tungsten filaments (300-2500 nm), and xenon arc lamps (160-2000 nm). An example can be seen in the case of the ALS SEC2000 spectrometer, which uses a tungsten-halogen for the VIS/NIR region, while deuterium and tungsten halogen lamps are used to extend into the UV/VIS region [36]. This system has previously been used to perform spectroscopic measurements on a VRFB system, obtaining absorbance vs SOC measurements in the 220-800 nm range [12].

This light can be split into its components using a monochromator such as a prism, which utilizes the relationship between speed and wavelength (dispersion) to refract colors into different directions. Photons have an energy given by:

$$E_{photon} = hv = \frac{hc}{\lambda} \tag{3.1}$$

where h is the Planck's constant, v is the frequency, c is the speed of light in a vacuum (299,792,458 m/s), and λ is the wavelength [37]. When light is travelling through a material denser than a vacuum (refractive index $(n) > 1$), its speed drops to $\frac{c}{n}$. Values for n depend on the wavelength and frequency (decreases with λ and increases with v), causing light to refract at different angles when passing through the interface between the two media.

More commonly a diffraction grating is used, where the grating spacing creates an interference pattern with maxima locations dependent on the wavelength of light. If the light is perpendicular to the diffraction grating surface ($\phi_m = 90°$), the behavior of the diffracted beam can be described using:

$$dsin\phi_m = m\lambda \tag{3.2}$$

where d is the spacing between the grooves of the grating, ϕ_m is the angle of the diffracted beam measured from a line normal to the diffraction grating's surface, m is the order of the principal maxima and λ is the wavelength of the beam leaving the grating at ϕ_m.

Grating design will impact this behaviour when the incident light ϕ_m is not perpendicular to the surface. Transmission gratings consist of a series of grooves which allow photons to diffract through the material, being described by equation 3.3. Reflective gratings do not allow photons to transmit through the material but are instead reflected off the surface at an angle given by equation 3.4. Blazed/ruled gratings are designed such that the grooves are oriented with a blaze angle γ (relative to a smooth surface) to provide maximum efficiency for a given m and wavelength. A Littrow configured grating is a blazed grating oriented such that the efficiency is highest $\phi_i = \phi_m$, with the Littrow configuration angle ϕ_L equal to the blaze angle γ. Blazed gratings and Littrrow configured gratings produce a beam governed by equations 3.5 and 3.6 respectively, where λ_D is the design wavelength [38].

$$d(sin\phi_m - sin\phi_i) = m\lambda \tag{3.3}$$

$$d(sin\phi_m + sin\phi_i) = m\lambda \tag{3.4}$$

$$dsin(-2\gamma) = m\lambda \tag{3.5}$$

$$2dsin\phi_L = m\lambda_d \tag{3.6}$$

Transmission gratings aid in minimizing alignment errors (lower alignment sensitivity) and have a comparable efficiency to blazed gratings (in the same range), although blazed gratings have higher efficiency at their design wavelength λ_D. Holographic gratings are lower efficiency than blazed gratings due to their sinusoidal groove

shape but may be better suited for sensitive measurements (blazed gratings are prone to periodic errors with large amounts of scattered light).

In a scanning spectrophotometer, the diffraction grating is scanned step-wise such that a point detector (ex a photodiode) can measure the intensity at each wavelength. A fixed grating is typically used in combination with an array detector such as a CCD. In this case, each wavelength is measured by a different detector in the array. In the case of a point detector, equations 3.2 - 3.6 can be used to calculate where the wavelength selector (slit) should be located for measurement of the correct wavelength (fixed grating), or how the grating should move in order for the point detector to measure multiple wavelengths. These equations may also be used to align a CCD and assist with matching the signals to the appropriate wavelength. In the case of an incident light source on the grating (equation 3.2), displacement from the center-line is given by:

$$y = \frac{m\lambda D}{d} \tag{3.7}$$

where y is the displacement and D is the distance between the grating and detector/surface [39]. These values may also aid in choosing a CCD with the proper detector area and focal length combination to match the grating's d spacing.

3.2 Sample Cuvette

When light passes through an object, some of the photons get reflected at the object surface/interface. Since it can maintain high transmittance at short wavelengths [34], typical cuvettes are made of quartz when investigating wavelengths in the UV-vis region [40]. Although cheaper, the transmittance of optical glass typically starts tapering off much earlier, and hence typically used for the visible region.

Absorbance is related to the amount of light incident on the flow cell (I_0) and light transmitted from the flow cell (I) through equation 3.8 [34]. For some applications,

absorbance scales linearly with the concentration and path length via Beer's law (equation 3.9) [13].

$$A = log(\frac{I_0}{I}) \tag{3.8}$$

$$A = abc \tag{3.9}$$

where A is the absorbance, a is the molar absorptivity, b is the path length, and c is the molar concentration. However, in an operational VRFB system, only the negative electrolyte obeys Beer's law. Analysis of the positive electrolyte is more complex as it only obeys Beer's law when very dilute (< 0.1 mol/L), and not during normal operation due to $VO^{2+}_{(aq)}/VO^{+}_{2(aq)}$ complexes forming at around 60% SOC [12, 13, 41].

3.3 Light Detection

A photodiode is a solid-state device than converts incident photon energy into electrical energy. A photodiode possesses a p-n junction, typically with a p-on-n configuration [42]. The p-n junction is typically produced through a photolithography process. For example, a silicon substrate is typically turned n-type (excess e^0) by doping it with donor impurities.

Thermal oxidation or chemical vapor deposition can then be used to grow a non-conductive SiO_2 layer on the surface. A photoresist is then applied, certain regions of which are chemically altered via exposure to UV before it is etched. This exposes regions of the SiO_2 allowing a pattern to be etched; and p-type region(s) with excess holes are created via doping with acceptor impurities (via gas or vapor or ion implantation). A metal such as Al can then be deposited, and a similar method can be used to etch it into contact(s) [43]. This can be seen schematically in Figure 3.2.

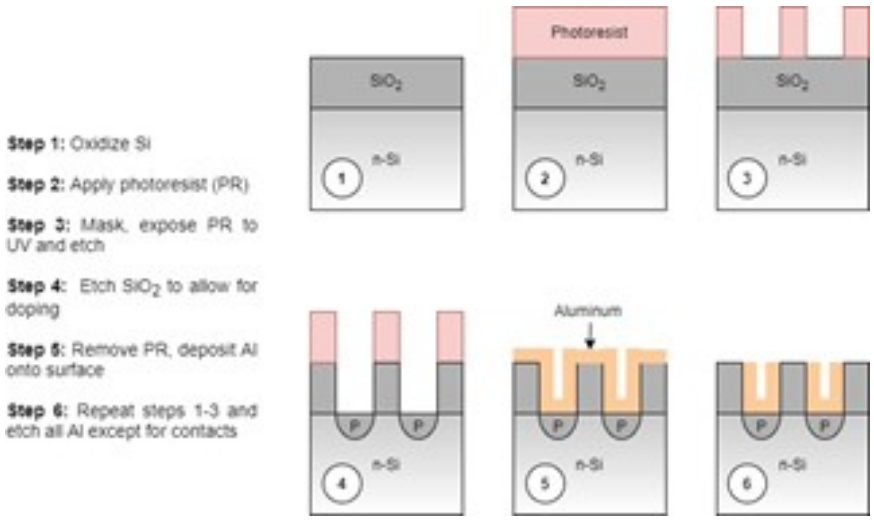

Figure 3.2: Fabrication of a p-n junction

The junction capacitance is an important parameter for determining the detector noise, as a smaller junction capacitance typically results in less noise [44]. The capacitance can be calculated from equation 3.10.

$$C_j = \frac{\epsilon_s A}{w} \tag{3.10}$$

where C_j is the junction capacitance, ϵ_s is the semiconductor permittivity, A is the area, and w is the width of the depletion region [45]. When a reverse bias voltage is applied, the capacitance can be reduced as described by:

$$C_j = \frac{C_{j0}}{\sqrt{1 + \frac{V_R}{\phi_b}}} \tag{3.11}$$

where C_{j0} is the capacitance at zero bias (calculated from equation 3.10), V_R is the reverse bias voltage, and ϕ_B is the built-in potential difference [44]. The potential difference is typically 0.6-0.7 V for Si and 0.3-0.35 V for Ge, and scales logarithmically with the amount of impurity ions that are added into the p-n junction (Figure 3.2) [46]. While higher reverse bias voltages are desirable to reduce the capacitance, the

upper bound is limited by the breakdown voltage, after which there is a sharp increase in photodiode current and permanent damage is likely [47].

The active material of a photodiode is a semiconductor which contains valence and conduction bands separated by an energy gap E_g. When the illuminated with photons with sufficient energy ($E_{Photon} > E_g$), electrons are excited from the valence to conduction band, causing current to flow proportional to the number of incident photons. Each material has a different responsivity to different wavelengths ($R_\lambda, (\frac{A}{W})$), and hence will produce different photocurrents (I_{Photo}) at the same incident power (P). This relationship is shown in equation 3.12 [47].

$$I_{Photo} = R_\lambda P \tag{3.12}$$

The total photodiode current (I) is given by the sum of the photocurrent and the dark current (I_{Dark}) which occurs under a reverse bias voltage in the absence of incident photons. The total photodiode current can be calculated with equation 3.13 where I_{Sat} is the reverse saturation current, q is the charge of an electron, k is the Boltzmann's constant, and T is the temperature in Kelvin [47].

$$I = I_{Photo} + I_{Sat}(e^{\frac{qV_R}{KT}} - 1) \tag{3.13}$$

By placing the photodiode into a circuit containing a resistive load, the photocurrent can be measured as a voltage. The choice of resistive load affects the frequency band width f_{BW} and rise/fall time t_r as governed by equations 3.14 and 3.15 respectively.

$$f_{BW} = \frac{1}{2\pi R_L C_j} \tag{3.14}$$

$$t_r = \frac{0.35}{f_{BW}} \tag{3.15}$$

where R_L is the load resistance [48]. In the case of very small photocurrent fluctuations, an amplifier may be used to increase the voltage response.

CCDs are composed of an array of p-n junctions, unlike photodiodes which typically contain one active junction. In a CCD, the gates above the p-n junctions are biased to create a potential well under the junction. When the shutter is opened, the incident photons generate electron-hole pairs and electrons begin piling up in the potential well. When the shutter is closed the gate electrodes are unbiased, and the electrons are moved to the vertical shift register by biasing the electrodes above it simultaneously. The electrons are then shifted row by row into the serial shift register after which the signal is amplified and the turned into a digital signal (intensity value between 0 and 255) [49].

3.4 Output Signal Analysis

In the case of a detector capturing full wavelength spectra, multiple spectrographs are generated between 0% and 100% SOC. Analysis must then be done to correlate absorbance data to SOC, of which there are multiple techniques. An example from [41] showed the development of a transmission curve database for multiple SOC's as a calibration step. After this was achieved, continued monitoring produced transmission curves that were compared against the database. The SOC value was then assigned based on the closest transmission curve match.

A study by [13] revealed a parabolic absorbance vs SOC graph when using a white light source (300 to 850 nm) on the positive electrolyte. The negative electrolyte showed an even simpler linear trend for single wavelengths. Similar results were obtained by [12], who fit linear curves to the absorbance vs SOC data at 433 nm, 600 nm and 750 nm for the negative electrolyte. For the positive electrolyte, an 'ideal absorbance' was determined based on Beer's law and the spectra of 0% SOC and 100% SOC chemistries. Measurements at mid-SOCs displays absorbance values in excess of Beer's law due to V(IV)/V(V) complexing. This excess absorbance is calculated

by subtracting obtained absorbance values from the ideal absorbance. This excess absorbance displays a parabolic relationship vs SOC for wavelengths of 600 nm and 760 nm.

In general, a relationship between absorbance and SOC can be obtained through simultaneous monitoring of the stack voltage/current and the voltage output from the photodiode/CCD light sensor. Coulomb counting is used to obtain SOC values from the stack's I-V curves, and these values can then be compared to photodiode voltage in order to assess the relationship between absorbance and SOC.

Chapter 4

Experimental Setup

4.1 VRFB System

A frame was constructed in order to hold all VRFB system components. This was achieved via the use of 6' and 2' 6105 anodized aluminum T-slotted quad framing rails (2" x 2" cross-section; part 47065T501, McMaster-Carr). Three platforms were created by affixing 2' rail segments to 6' segments using corner brackets (part 47065T237, McMaster-Carr), or cheaper corner concealed brackets (part 5537T315, McMaster-Carr) where strength requirements are lower. These platforms are affixed horizontally between 6' vertical rail segments using diagonal braces (top/bottom platforms; part 47065T187, McMaster-Carr) or the aforementioned corner brackets (middle platform). This setup can be seen schematically in Figure 4.1, with the solid black lines representing the 6' rail segments (2' segments into the page).

The positive and negative electrolyte are stored in 22 gallon (83L) polyethylene tanks (part 3662K33, McMaster-Carr) located on the bottom platform. In some experiments, the electrolyte tanks are connected via $\frac{1}{4}$" inner diameter santoprene tubing (part 51225K29, McMaster-Carr) as illustrated by the orange line in Figure 4.1, creating a hydraulic shunt between the two tanks. This allows for simple rebalancing of electrolyte volumes and oxidation states. Prior to testing, the electrolyte tanks are first purged with grade 4.8 nitrogen (99.998 % pure) in order to reduce side reactions such as the air oxidation of V^{2+}.

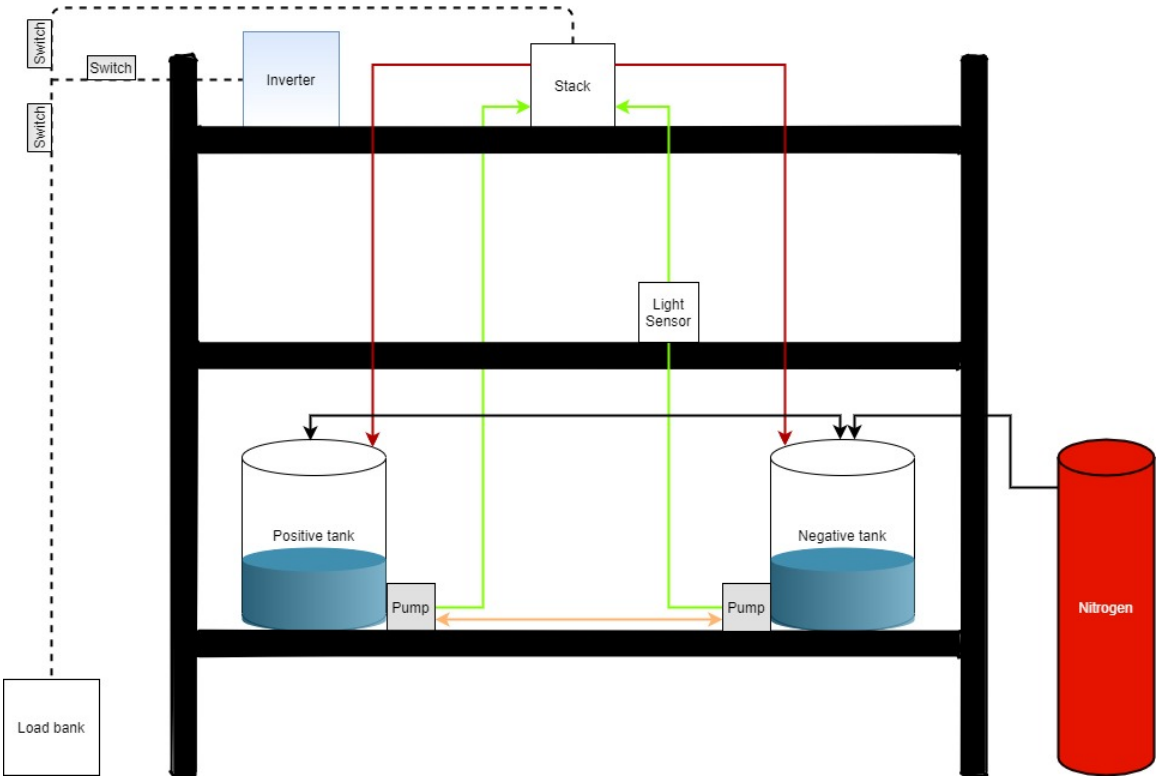

Figure 4.1: Setup of the VRFB system

Magnetic drive pumps (part INTG3-572, AOP Technologies) are used to pump the electrolyte from the tanks into a 2.5 kW stack (VFBS 40, Volterion) located on the top platform via $\frac{1}{2}$" inner diameter santoprene tubing (green line in Figure 4.1; part 51225K43, McMaster-Carr). The electrolyte is then returned to to the electrolyte tanks via $\frac{1}{2}$" tubing as shown by the red line in Figure 4.1). The pumps are powered via a 24 V 211 W AC/DC converter (Digi-key 1866-3332-ND). Flowmeters (McMaster-Carr 9687K11) are placed inline prior to entering the stack and used to monitor the electrolyte flowrate entering the stack. The pressure drop across the stack is monitored with 15 psig analog pressure sensors (Digi-key BPS140-HG015P-1SGCT-ND) located at the stack inlets/outlets. The locations of these sensors may be seen in Figure 4.2.

Initial experiments were performed using startup cylinders using a smaller amount of electrolyte in order to minimize the chance of leaks and to maintain a constant

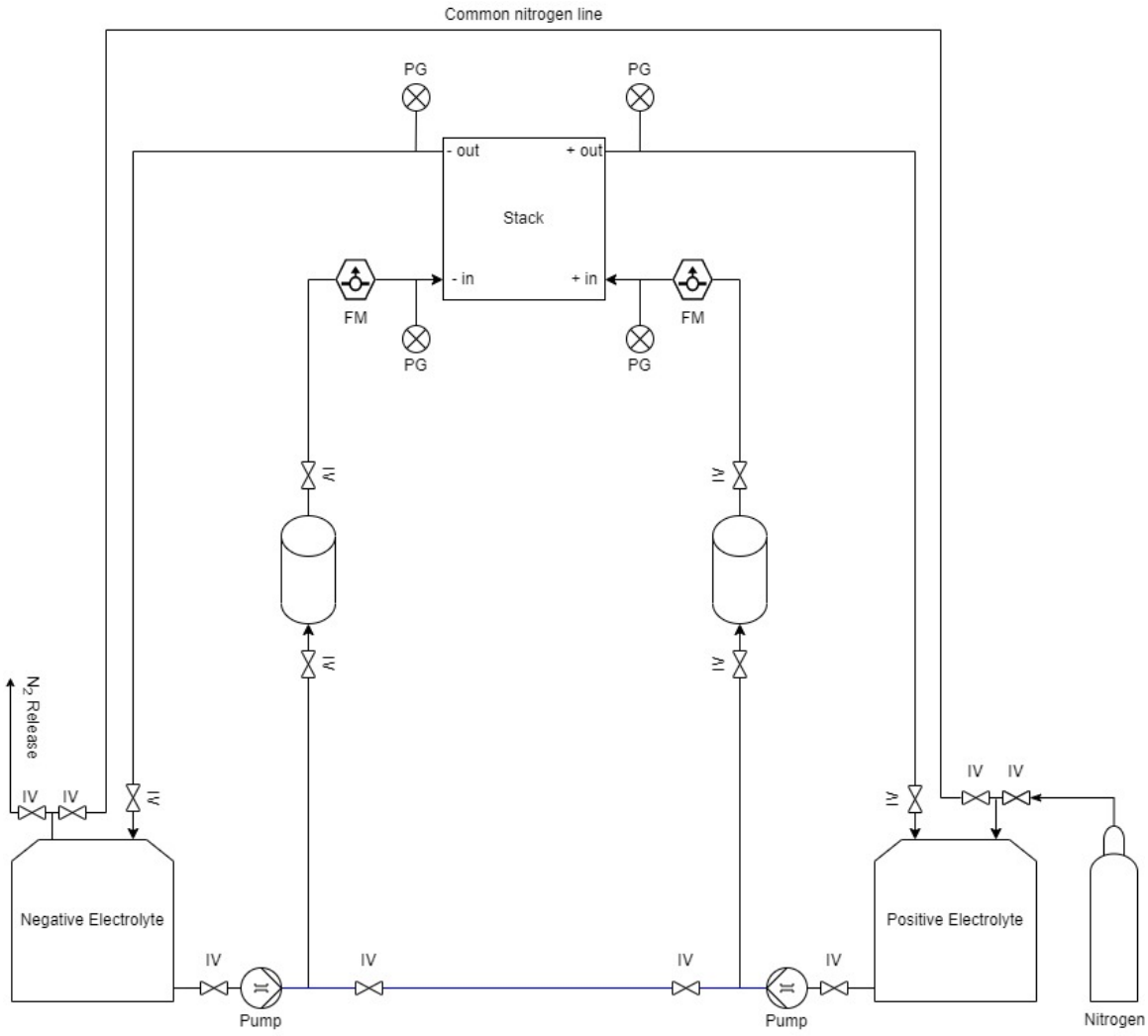

Figure 4.2: Piping and instrumentation diagram of the VRFB system showing the locations of pressure gauges (PG), isolation valves (IV), and flowmeters (FM)

6" pump head. The cylinder cavities were constructed from 6" outer diameter, 5.75" inner diameter, 1' long impact-resistant polycarbonate tubes, giving them a maximum volume of 5.1 L per cylinder. Chemical-resistant epoxy was used to adhere caps to the cylinder (7" diameter, $\frac{1}{4}$" thick clear acrylic disks). The startup cylinders were machined to allow bulkhead fittings (2-$\frac{7}{8}$"" long, $\frac{3}{4}$" NPT) to be installed on the top cap and near the bottom of the cylinder's body. These acted as the cylinder inlet/outlets respectively by using $\frac{3}{4}$" NPT barbed fittings to allow for the connection of $\frac{1}{2}$" santoprene tubing.

These cylinders were placed on the middle platform inline prior to stack inlets (green line in Figure 4.1). In the case of tests performed using both startup cylinders and main tanks, it can be noted that the pumps are used at the base of the startup cylinders as opposed to the base of the large 83 L tanks as implied in Figure 4.2. Each startup cylinder is then filled with approximately 4 L of electrolyte (with the remainder of the utilized electrolyte split among the large tanks), allowing a constant 6" pump head to be maintained. For the testing of smaller amounts of electrolyte (approximately 8 L), the startup cylinders may be easily isolated from the large tanks by altering tube connections with the large tanks are bypassed and the electrolyte rebalancing tube connects the startup cylinders.

4.2 SOC Detector

4.2.1 Sample Cuvette

The flow cell (Figure 4.3) was created with 6" x 6" x $\frac{1}{2}$" thick acrylic sheets as endplates to provide structural support while allowing for 92% (visible) light transmission through each sheet. In order to install electrolyte inlets/outlets, holes are machined into one endplate and $\frac{1}{2}$" tube adapters are affixed using a clear-dry silicone gel.

The flow structure consists of hollow silicone gasket(s) to allow for electrolyte flow while ensuring a watertight seal is maintained with the endplates. A thin acrylic sheet may also be placed between two gaskets to provide larger optical path options while maintaining mechanical strength and a proper seal. This concept was used to create the $\frac{1}{4}$" flow cell seen in Figure 4.3. The optical path through the electrolyte is dictated by the thickness of the internal gaskets/acrylic sheets, while the electrolyte flow pattern is dictated by their shape. The internal gaskets/sheets are hollowed out in a U-shaped pattern to allow for proper electrolyte flow through the cell while reducing the likelihood of dead zones within the cell. The flow structure is compressed between the $\frac{1}{2}$" acrylic end sheets using six corrosion resistant bolts ($\frac{1}{4}$" diameter).

These bolts are placed alongside the outside edges of the flow cell, approximately 1.5" away from eachother and centered $\frac{1}{2}$" away from the edge.

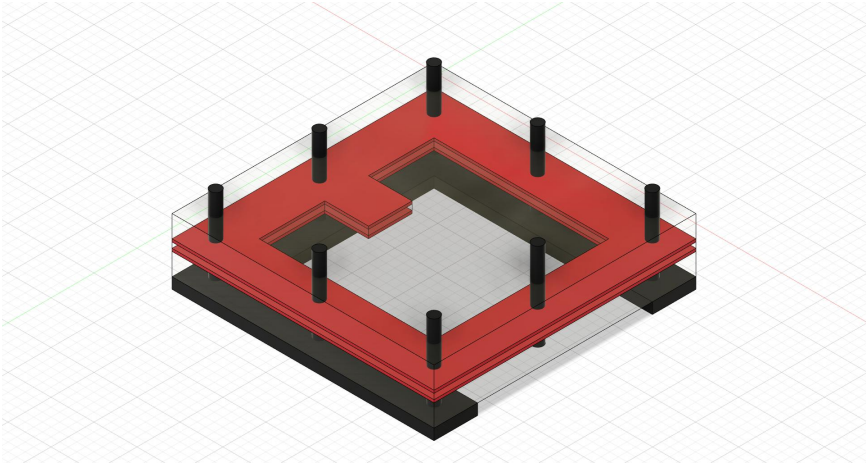

Figure 4.3: Construction of a clear flow cell with housing for ambient light reduction

Electrolyte is pumped through the flow cell from the electrolyte tanks prior to entering the VRFB stack. The electrolyte enters and exits the cell through $\frac{1}{4}$" tube adaptors located on the face of one endplate on either side of the hollow U-pattern (not shown in Figure 4.3). The use of clear acrylic endplates and a hollow flow structure creates an unobstructed view through the flow cell, allowing for continual optical monitoring of electrolyte being pumped through the cell.

The simplistic layered design allows for easy manipulation of the shape and size of the cell's internal cavity between experiments. Three configurations were tested with interior cavity thicknesses of $\frac{1}{4}$", $\frac{1}{8}$", and $\frac{1}{16}$". For creation of the $\frac{1}{4}$" flow cell cavity, a $\frac{1}{8}$" acrylic sheet was sandwiched between two $\frac{1}{16}$" silicone gaskets. The $\frac{1}{8}$" configuration was done via removal of the acrylic sheet, while the $\frac{1}{16}$" configuration simply consists of one $\frac{1}{16}$" gasket.

4.2.2 Light Detection

The initial photodiode circuit design simply consisted of a photodiode, a load resistor, and a noise filter milled onto a 1.5 mm thick copper clad PCB (B07TWHLMVP YUNGUI) (LM741 electron components). The photodiode (FD11A Thorlabs) was a

1.1 mm x 1.1 mm Si sensor with a maximum responsivity of 0.6 A/W [50]. The noise filter consists of a 0.1 µF capacitor and 1 $k\Omega$ resistor under a reverse bias of 24 V. Photodiode current was converted into voltage readings under a load resistance of 100 $k\Omega$. Lead wires (for biasing the noise filter and monitoring photodiode voltage) are connected to the PCB via screw terminals (TN-T03G Tnisesm), resulting in a setup shown in Figure 4.4. To improve data output from the photodiode, the circuit design can be modified to include an operational amplifier (LM741 electron components). This design change is reflected in Figure 4.5.

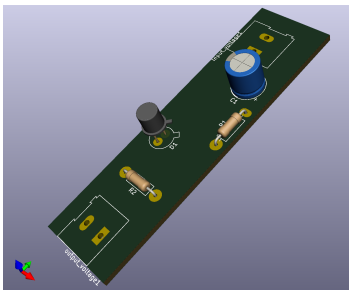

(a) PCB layout

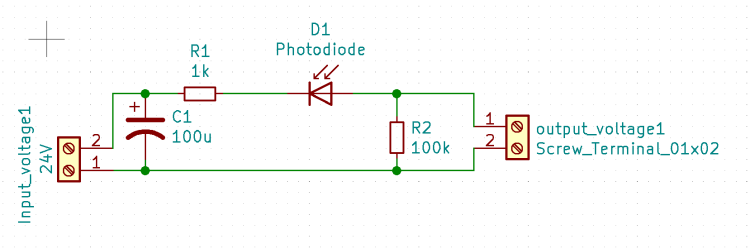

(b) Circuit design

Figure 4.4: PCB without amplifier

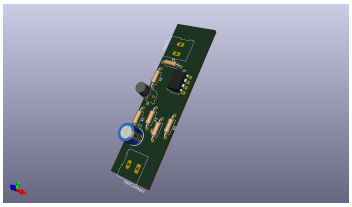

(a) PCB layout

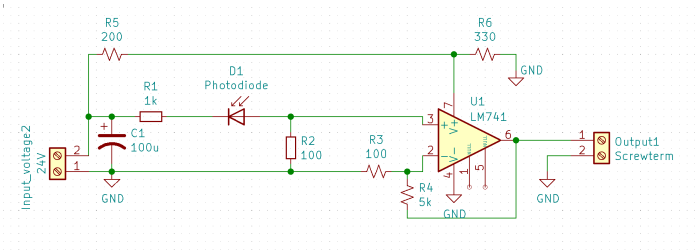

(b) Circuit design

Figure 4.5: PCB with amplifier

In order to minimize measurement errors, an opaque housing is used to reduce ambient light reaching the detector. In initial experiments, the photodiode circuit was placed in a 2" deep plastic tray placed under the flow cell. However, the addition of a black acrylic sheet to the bottom of the flow cell (as in Figure 4.3) allows the photodiode to be placed directly in contact with flow cell endplate. To facilitate this, the photodiode may be enclosed in an additional grey housing as shown in Figure

4.6. The closer proximity to the light source increases the signal/noise ratio via a reduction of both ambient light and the light source's spot size on the PCB (less beam divergence after exiting the cell), while improving consistency between tests by allowing for simpler alignment of the light source and detector.

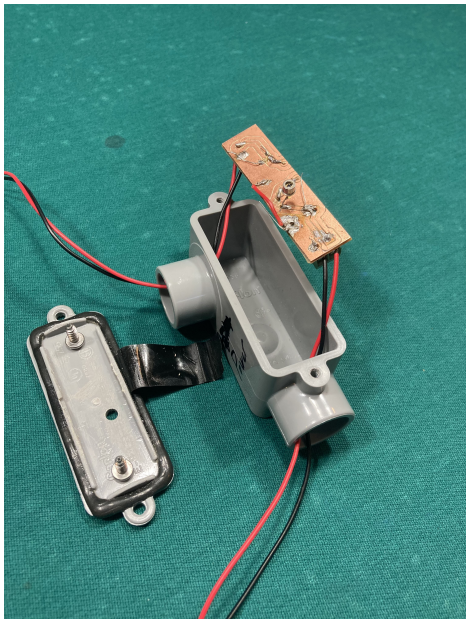

Figure 4.6: Experimental view of photodiode PCB with amplifier

The top of the flow cell is illuminated with a 550 lumen (Duracell) white light source, and electrolyte is pumped through the flow cell. Light transmitted through the electrolyte is detected by the photodiode, producing a voltage response. This voltage response is monitored using an analog input on the National instruments USB-6211 multifunctional I/O device. Data is obtained during battery cycling and compared to IV curves for analysis. Further details regarding testing procedures may be found in section 4.4.3.

4.3 System Cost

This section outlines the costs associated with the VRFB system/project. Costs associated with the SOC sensor are contained in section 4.3.1, with other VRFB system costs (electrolyte, tanks, tubing, frame etc) being discussed in section 4.3.2.

Full lists of item costs are tabulated within Appendix A.

4.3.1 SOC Sensor

Construction of the flow cell is relatively inexpensive, varying based on the optical path length desired. Basic costs for each configuration is approximately $55.68 USD (external end plates, inlets/outlet adaptors, nuts/bolts/washers). Flow cells with optical paths of $\frac{1}{4}$", $\frac{3}{16}$", $\frac{1}{8}$", $\frac{1}{16}$", $\frac{1}{25}$", $\frac{1}{50}$", and $\frac{1}{100}$" may be constructed by adding gaskets and/or acrylic sheets between these endplates (as is the case with the $\frac{1}{4}$" flow cell shown in Figure 4.3), with costs ranging from $78.60 to $114.87.

The photodiode circuit is milled onto a 1.5 mm thick PCB board and screw terminals affixed on either end to allow for voltage measurements and the application of a 24 V bias voltage with output/input leads ($25.98 USD). The chosen FD11A Si photodiode ($14.58 USD) measures the light transmitted through the flow cell via a $9 550 Lumen Duracell light source. Resistors and a capacitor are integrated into the circuit to create a noise filter and load resistance. In the case of the utilized circuit design (shown in Figure 4.4), this results in a total cost of $57.56. An operational amp and additional resistors are required for the circuit design shown in Figure 4.5, resulting in an increased cost of $63.8.

Individual costs for each item are summarized in Table A.1 (located in Appendix A.1). Overall, construction of a SOC sensor with an amplified signal and a 1/100" optical path length flow cell costs approximately $151.4 ($78.6 for the flow cell, $63.8 for the photodiode circuit, and $9 for the light source).

4.3.2 VRFB System

A full list of the VRFB system costs can be found in Tables A.2/A.3 located in Appendix A.2. The vanadium electrolyte was the most significant cost of the project, being approximately $2955.79 USD for 100 L of electrolyte. This was followed by the stack at approximately $2255 USD and the inverter/charger at approximately $1579

USD.

The frame and other structural components of the VRFB system costed a total of $1551.38 USD. In order to store the bulk of the electrolyte, two large 83 L polypropylene tanks were equipped with fittings, costing $823.36 USD. Startup cylinders may be constructed for approximately $269.26 USD for storing of smaller electrolyte volumes (up to 5 L per cylinder) at a constant pump head. Auxilliary equipment such as thread tape, hand pumps, funnels, spill control trays costed $976.09 USD. Barbed fittings and other connectors costed approximately $236.23 USD, while tubing and clamps costed an additional $309.62 USD.

The pump and its required electronics (switches, fuses, power supply) costed approximately $603.53 USD, with $104.13 USD being required for other auxiliary electronic costs (wiring, spade terminals etc). The flowmeter and pressure sensors costed approximately $540 USD, with measurements being obtained using a $1116 USD National instruments USB-6211 multifunctional I/O device.

Periodic costs included disposable gloves, DI water for occasional testing and cleaning of the stack and equipment, grade 4.8 Nitrogen (99.998% pure). In total, $152.73 was spent on safety equipment, $38.9 on Nitrogen (two T-size cylinders), and $100.46 on DI water.

The total cost of the VRFB system was approximately $13600 USD. The electrolyte and stack only constitute about 38% of the total system cost, with the frame and electrolyte tanks (fitted with inlet and outlet adaptors) constituting about 18% of the cost. It is important to account for this during the design of a VRFB system, as it is a general trend seen seen in VRFB installations.

4.4 Testing

4.4.1 Startup Cylinders

The charge process consists of both a constant current 'bulk' regime, and a constant voltage 'absorbance' regime. Charging is first done in bulk mode with a constant maximum current of 10 A until a 58 V stack voltage was reached. The current is then steadily reduced such that a 58 V stack voltage is maintained ('absorbance mode'), until a minimum of 1.5 A is reached.

Discharging was done through a load bank with a constant 10 Ω resistance. This results in a 5.5 A maximum discharge voltage. While the nominal stack operating range is 40-62 V, discharging is done until reaching atleast 30 V in order to preserve electrolyte lifetime (by reducing the likelihood of V^{2+} oxidation between experiments) and consistency between tests. A 40 V cutoff voltage (normal stack operating region) is used for the calculation of SOC and discharge capacity to maintain consistency during data analysis while ensuring results are comparable to literature values.

A total of 19 cycles were performed utilizing approximately 4 L of anolyte and catholyte, for a total of 8 L. The electrolyte was stored in small custom designed startup tanks (1 foot tall cylinders with a 5.75"/6" inner/outer diameter) with 5.1 L capacities. The results from these experiments are contained within section 5.1.

In order to mitigate volume transfer from the positive to the negative electrolyte reservoir, three types of electrolyte rebalancing techniques were employed. The first technique was conducted manually - excess electrolyte in the anolyte reservoir was transferred back into the catholyte reservoir by means of a beaker until volumes were once again balanced. Results from this method are found in section 5.1.1.

Further volume rebalancing was done by means of a tube connecting the reservoirs, with initiation and completion of the process controlled via an on/off valve. Prior to cycle 13 the valve was opened, volumes were allowed to reach an equilibrium, and then was closed again (essentially being an improvement on the manual rebalancing

process). A similar approach is used prior to the final cycle, except the valve is left open for the duration of the test. An additional modification to the final two cycles was the reduction of the charge current to 5 A such that the charge and discharge process have similar maximum currents. Results from these experiments are found in section 5.1.2.

4.4.2 Large Tanks

Experimental results utilizing a higher electrolyte volume can be found in section 5.2. Approximately 20 L of electrolyte is used per tank, for a total volume of 40 L present within the VRFB system. The anolyte and catholyte are stored in two 83 L tanks which are purged with Grade 4.8 nitrogen prior to battery cycling in order to avoid air oxidation of V^{2+}.

Charge current

VRFB cycling was initially conducted with a 15 A maximum charging current before being increased to 30 A. For all cycles, charging was performed to a 62 V stack voltage, and was terminated when the current was below 1.5 A. Similar to experiments performed on the startup cylinders, discharging was done through a load bank with a constant 10 Ω resistance.

Results obtained with a 15 A max charging current are shown in section 5.2.1. These 21 cycles are compared to 6 cycles performed at a maximum current of 30 A in section 5.2.2.

Discharge current

To test the effect of the discharging current, discharge is done through a 1.4 Ω resistor set, resulting in maximum currents of 40-45 A. As such, a 40 A maximum charge current was chosen to be employed. The charge process was once again done with a 62 V maximum stack voltage, and was terminated when the current was below 1.5 A. Due to the higher losses during the discharge process, discharging was performed until reaching a stack voltage below 15 V, which corresponds to an SOC

below 0% and an elimination of V^{2+} in the anolyte. Results from these 8 cycles are located in section 5.2.3.

SOC-OCV measurements:

The battery was initially charged with a maximum current of 20A until reaching 62 V. It was then left to rest for 40 minutes before being discharged in 5 minute segments through a 10 Ω resistor (5.5 A max). Each 5 minute discharge segment was followed by a 5 minute relaxation period to allow for voltage stabilization. This 5 minute relaxation window allows the stack voltage to reach a steady state value, and the OCV to be calculated.

Based on observations made from initial experiments, the test was then changed such that more data points could be obtained at high and low SOCs. Initial relaxation time after initial battery charging was reduced from 40 to 20 minutes, while the relaxation time between discharge segments was decreased to 2 minutes until dropping below 25% SOC. To maximize the number of data points that can be retrieved while accomodating for time constraints, the charge current was increased slightly from 20 A to 25 A. Results from these experiments are contained within section 5.2.4.

4.4.3 SOC Sensor

Three flow cell configurations with interior cavity thicknesses of 1/4", 1/8", and 1/16" were tested on the anolyte/catholyte individually. The flow cell is placed inline between the stack and electrolyte reservoir to determine the absorbance of electrolyte in question prior to entering the stack. Tube connections were made such that electrolyte from the anolyte/catholyte reservoir enters the flow cell through the left leg of the U-shape cavity, flows counterclockwise through the cell, and exits to the stack through the top of the U-shaped cavity's right leg.

The 550 lumen light source is placed directly on the top of the flow cell to illuminate electrolyte flowing through the lower portion of the cell's U-shaped cavity. The photodiode circuit (Figure 4.4) is positioned underneath the flow cell directly

opposite the light source in order to monitor light transmitted through the cell. The photodiode is placed under a reverse bias via a 24 V power source (Digi-key 1866-3332-ND), and its voltage output is monitored via an analog input on the USB-6211 I/O device.

The photodiode voltage was monitored over the course of a charge/discharge cycle to calibrate the sensor and assess the suitability of this technique for monitoring of the positive/negative electrolytes. Each experiment was performed using a 30 A max charge process with a 62 V/1.5A cutoff. Discharge was done through a 1.4 Ω resistor set, resulting in maximum discharge currents in excess of 40 A. These results are presented in section 5.3, with results from the negative and positive electrolyte being contained in sections 5.3.1 and 5.3.2 respectively.

Chapter 5

Results and Discussion

5.1 Startup Cylinders

5.1.1 Manual Rebalancing

Charging was done with a maximum current of 10 A until reaching a max voltage of 58 V and stopped after the current has decreased below 1.5 A, while discharging was done at a constant 10 Ω resistance until the stack voltage was below 30 V. An approximate total volume of 8 L was utilized (4 L per startup cylinder). Voltage, current, and power data was obtained for 12 cycles and shown in Figure 5.1, with a-c and d-f representing the charge and discharge process respectively.

Capacity and efficiency values for each cycle can be extracted through integration of the cycle data in Figure 5.1. For example, energy input is calculated through integration of Figure 5.1 b) and c), yielding results in Ah and Wh respectively. The same can be process can be used to extract output energy using Figure 5.1 e) and f). The extracted capacity data is plotted in Figure 5.2, also depicting the efficiency and capacity change per cycle.

Over the course of battery cycling, the electrolyte volume in the positive cylinder was observed to decrease and be transferred into the negative cylinder. Net volume transfer towards the negative tank is common with an AEM and was observed when rebalancing was done manually, causing the positive electrolyte to possess a smaller amount of vanadium at a higher SOC than that contained in the negative tank. As

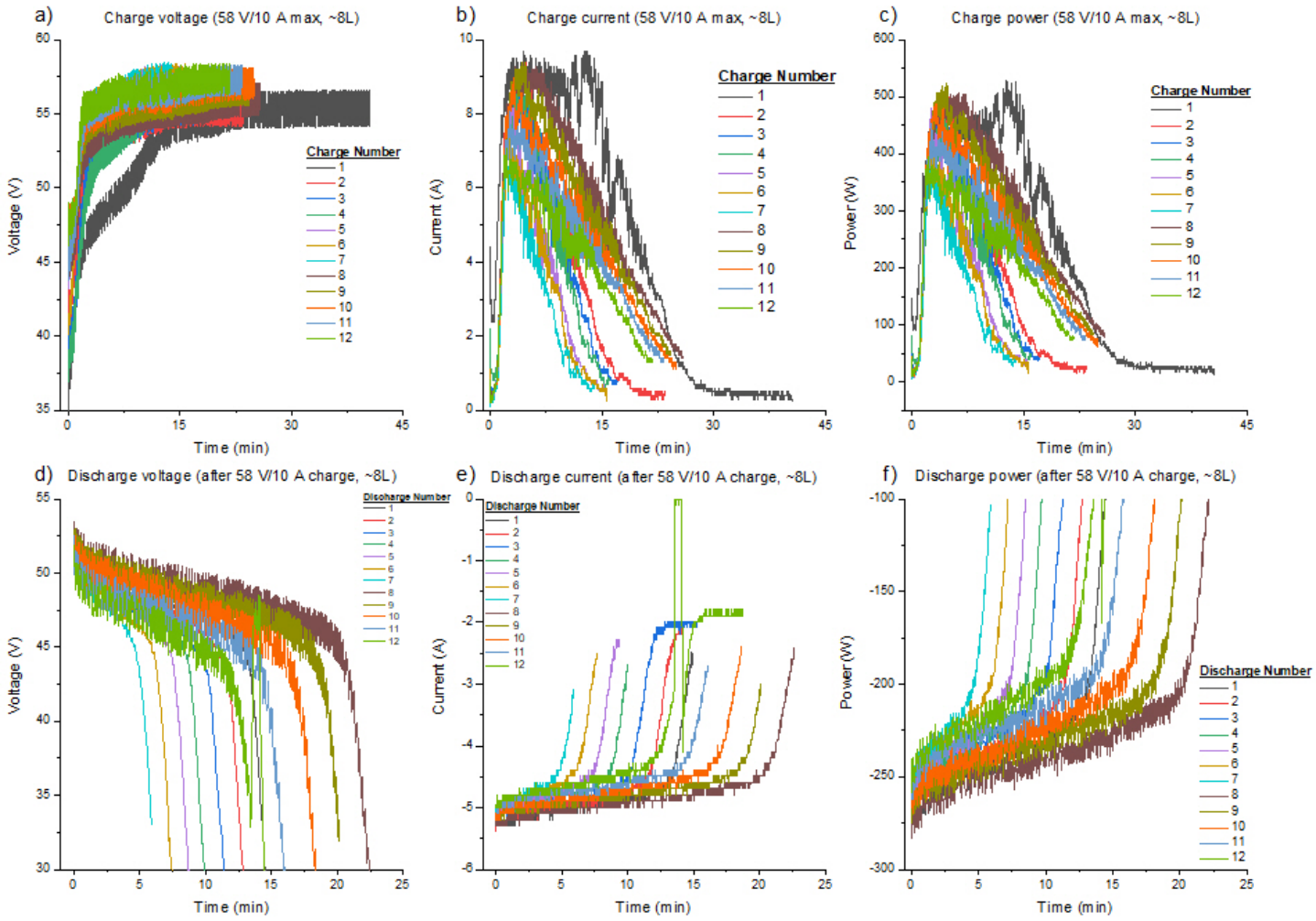

Figure 5.1: VRFB cycling data utilizing startup cylinders (4 L per cylinder) and a manual rebalance prior to cycle 8. a) terminal voltage, b) current, and c) power, measured during VRFB charging until 58 V (10 A max). d) terminal voltage, e) current, and f) power, measured during VRFB discharge through a 10 Ω load bank

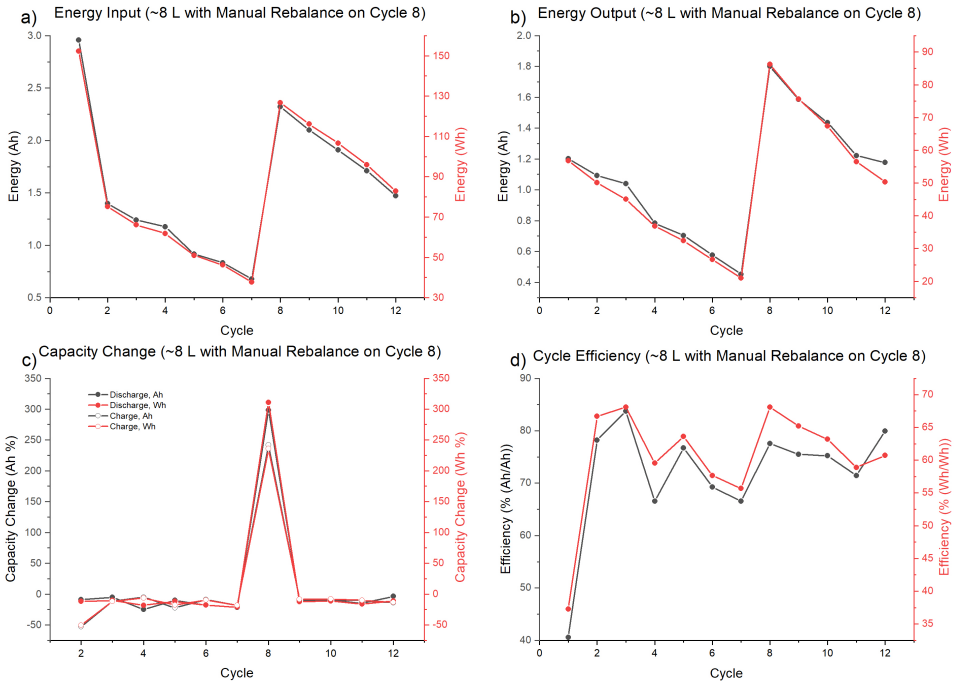

Figure 5.2: Extracted data from cycling of startup cylinders (4 L per cylinder) with a manual rebalance prior to cycle 8. a) Energy input b) energy output c) capacity change % d) cycle efficiency after a 58 V charge (10 A max) and discharge through a 10 Ω load bank

a result of this process, 2/3 of the discharge capacity was lost over the course of the first seven cycles.

In order to mitigate this, the electrolyte volumes need to be rebalanced, the effect of which can be seen in cycle 8. 100% capacity recovery is not achieved due to the fact that rebalancing is being done with a simple manual method by transferring electrolyte between tanks (the anolyte and catholyte are not fully mixed, and rebalancing of the oxidation states is suboptimal). The electrolyte rebalancing process may also be done automatically via a tube connecting the two electrolyte tanks. This concept is tested in the following section, as well as an improvement on the manual rebalancing process.

5.1.2 Automatic Rebalancing

A hydraulic shunt connecting the tanks (ex a small diameter tube with a needle valve) may be used to mitigate these bulk water transport issues, with volume differences causing electrolyte to flow across the shunt until a pressure equilibrium is re-achieved [11]. This allows the rebalancing process to be done continuously and accurately with minimal operator input.

In this experiment, a simple shunt was created with a 1/4" diameter tube, with PVC on/off valves in order to start/stop the potential for electrolyte transfer. Six additional cycles were performed with capacity values plotted in Figure 5.3a). These results demonstrate the ability for symmetrical capacity losses to be mitigated via simple remixing of the electrolytes. Comparisons to the manual rebalancing process (Figures 5.3 b) and c)) illustrates that this automatic mechanism is able to achieve a comparable capacity gain versus manual transfer/rebalancing of electrolyte volumes between experiments.

It can be noted that the manual rebalance at cycle 13 was done via opening of the automatic rebalancing tube for a short time. This resulted in a discharge capacity recovery comparable to the previous manual rebalancing method. However, mixing of the electrolytes results in a loss of energy stored in the electrolyte. This is be observed via an increase in charge energy and large reduction in cycle efficiency (Figure 5.3d), while the increase in charge energy observed in cycle 15 is an artifact caused by absorbance mode charging beyond the 1.5 A cutoff current (which slightly reduced the capacity decay for the cycle).

A similar efficiency loss is seen in cycle 18, where the automatic rebalancing tube was left open for the duration of the test. Capacity recovery was not as high during this cycle due to the fact that electrolyte transfer through the rebalancing tube occurs throughout the cycle. This results in self discharge according to equations 2.19, 2.20, and 2.21.

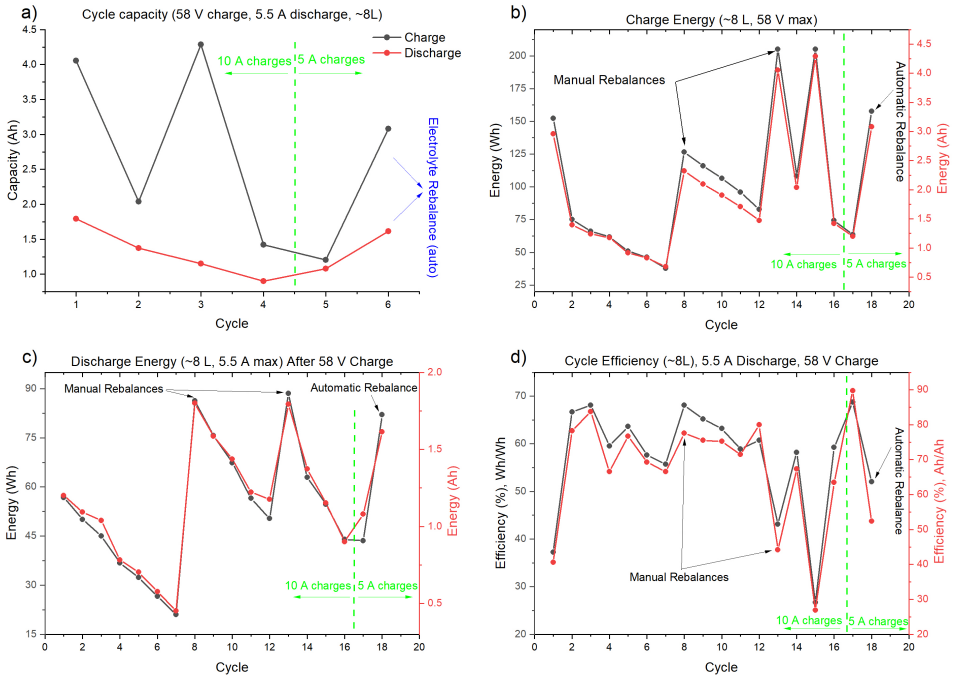

Figure 5.3: Effect of automatic/manual rebalancing utilizing startup cylinders (4 L per cylinder). a) Capacity recovery from automatic rebalancing, comparison to manual rebalancing in terms of b) Charge energy, c) discharge energy and d) cycle efficiency after a 58 V charge (10 A or 5 A max) and discharge through a 10 Ω load bank

A drawback of the current method is reduced cycle efficiency due to self-discharge through the rebalancing tube if the on/off valve is left in the open position during testing. To mitigate this, the on/off valve may be replaced with a needle valve such that the electrolyte may only flow when there is a pressure differential driving the electrolyte in one direction [11]. This will assist in the reduction of self-discharge processes caused by diffusion of vanadium ions across the rebalancing tube, hence increasing the efficiency and usable capacity of the VRFB system.

In addition to this method allowing for successful recovery of capacity loss due to bulk volume transfer, it also provides many benefits over manual rebalancing. The automatic rebalancing process can be initiated/suspended simply by closing an on/off

valve, not requiring any system disassembly (tube removal etc) as is the case with the manual rebalancing method. This simplified process allows for increased operator safety and a decreased likelihood of electrolyte leaks.

5.2 Large Tanks

These experiments utilize a 20 L volume of anolyte and catholyte stored in two 83 L tanks, with a nitrogen purge being done before charging in order to avoid air oxidation of V^{2+}. As 20 L of electrolyte is used per tank, the capacity is expected to be approximately five times higher than was obtained in Section 5.1 with 4 L of electrolyte per reservoir (due to the linear relationship between capacity and electrolyte volume).

5.2.1 15 A Charge Current

A 15 A charge current was used until reaching 62 V. The stack was then discharged through a load bank with a constant 10 Ω resistance until below 40 V as can be seen in Figure 5.4 a) and b). The initial discharge voltage near 100% SOC (Figure 5.4 b) is higher than that obtained previously in section 5.1.1 (Figure 5.1d). This is due to the increased charge voltage cutoff from 58 V to 62 V, allowing the electrolyte to be charged up to values closer to 100% SOC than was previously obtained. Although the charge voltage was also increased from 10 A to 15 A, large deviations in the discharge curves are not expected - with the primary influence being on the charge power and cycle efficiency due to the increased overpotentials.

Additionally, the stack voltages obtained during discharge were observed to decay in a much smoother fashion than those obtained in Section 5.1.1. This is primarily due to the large increase in electrolyte volume from 8 L to 40 L. The 5-fold increase in electrolyte volume as well as the increased charge voltage cutoff caused the average discharge time to increase from 15 minutes to approximately 90 minutes due to the increased battery capacity. Not only does this allow more data points to be taken over

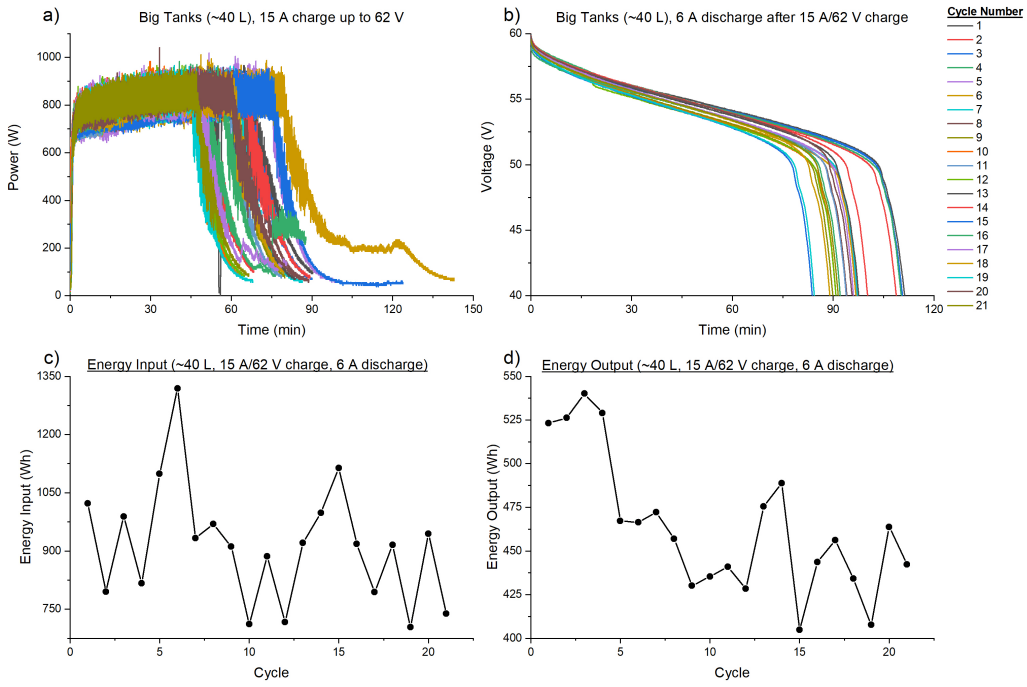

Figure 5.4: VRFB cycling data utilizing big tanks (40 L) with an automatic rebalancing tube. Cycle a) charge power, b) discharge voltage, c) energy input, d) energy output

the course of cycling, oxidation state concentration fluctuations due to bulk water/ion transfer, incomplete electrolyte mixing, etc are less pronounced.

Due to the use of the automatic rebalancing tube, the capacity was not observed to decay as significantly over the course of repeated cycling (Figure 5.4). Neglecting the first four cycles, the capacity was only observed to fluctuate by 75 Wh (25%), primarily being caused to small variations in electrolyte flowrate, temperature, electrolyte leaks, and input energy between tests. This is in contrast to the 75% capacity fluctuations seen in Figures 5.2 and 5.3, which were caused by bulk water transport through the membrane (and exacerbated by the lower electrolyte volume).

5.2.2 30 A Charge Current

Testing was performed in the same manner as Section 5.2.1, except the charge current was doubled. A 30 A charge current was used until reaching 62 V, then discharged through a 10 Ω load bank until below 40 V. Six cycles were performed, with results being plotted in Figure 5.5, and capacity values compared to the 21 cycles obtained using a 15 A charge current.

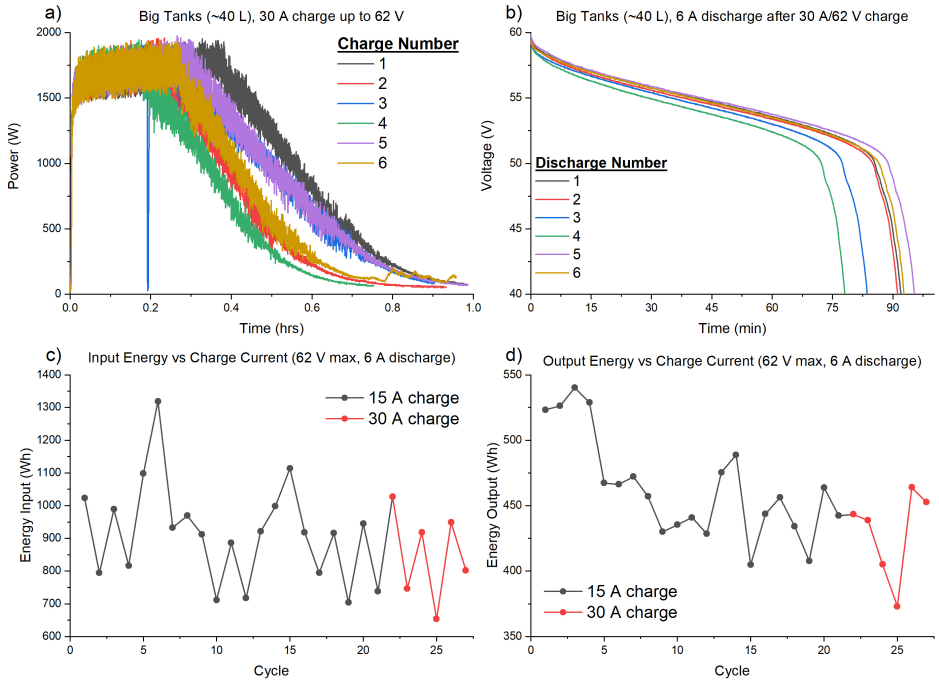

Figure 5.5: VRFB cycling data utilizing big tanks (40 L) with an automatic rebalancing tube, comparing two different charge currents. Cycle a) charge power, b) discharge voltage, c) energy input, d) energy output

Increasing charge current from 15 A to 30 A appears to cause the stack's Ah output to decrease at a slightly faster pace (-0.9% Ah/cycle at 15 A, -1.27% Ah/cycle at 30 A as seen in Figure 5.5 d)). As only 6 cycles were performed at 30 A, these values are heavily affected by fluctuations as mentioned in Section 5.2.1. A fluctuation of this type was observed between cycles 25-26, which are separated by a two-day window

where experiments were not performed.

However, this behaviour of increased capacity loss can be expected due to the increased charging current. As the maximum current was doubled, the charging time is approximately half as long as previously. As the automatic rebalancing tube has a small diameter (to prevent unwanted self-discharge processes from occurring), the reduced charging time was observed to hinder its ability to mitigate bulk water transport between the electrolyte tanks. This capacity may be recovered periodically by giving the tanks sufficient time to re-achieve a volume equilibrium (when near 0% SOC to avoid the loss of stored energy), as was done between cycles 25-26, or via redesign of the rebalancing mechanism.

In addition, the increased charge current may increase the likelihood of unwanted side reactions from occurring, such as oxygen and hydrogen evolution (equations 2.4 and 2.5). These reactions may cause a asymmetrical capacity loss in the system due to H^+ formation/production, which causes a shift in the measured voltage and is unable to be mitigated via electrolyte rebalancing.

5.2.3 Discharge current

Previously, discharging was performed using a 10 Ω load bank to achieve maximum currents of about 10 A. In this case, a 1.4 Ω resistor set is used to achieve max currents in excess of 40 A. The charging current is also increased to 40 A, and 8 charge/discharge cycles were performed. Charging power and discharge voltage results from these cycles are shown in Figure 5.6. Although a higher charge current was used, the charge times that are observed are quite similar to those obtained when using a 30 A charge current. The high current gives rise to a larger overpotential, which reduces the amount of time that charging is performed in bulk mode before switching into constant voltage absorption mode.

However, the voltage profile during the discharge process deviates from that which is predicted by the Nernst equation. This is driven in part by the increase in ohmic

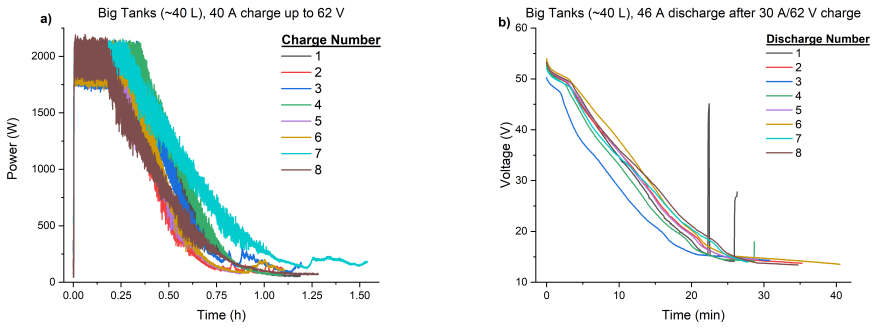

Figure 5.6: VRFB cycling data utilizing big tanks (40 L) with an automatic rebalancing tube and resistors for 30 A max discharge current. a) charge power, b) discharge voltage

losses associated with the increase in current. Another possible cause is that the flowrate is too low to withstand the large increase in power, as there is a minimum flowrate for a given current (derived from Faraday's law of electrolysis). In this case flowrate was maintained around 6 L/min, above what is required for the current densities utilized in this experiment. Additionally, a region of constant current would be expected at high SOCs if power output was restricted by the vanadium ion concentration, which was not observed.

These observations suggest that the power/capacity ratio is too high, and that the volume of electrolyte should be increased above 20 L/reservoir when attempting to use large 40 A currents. Further evidence can be observed in the seventh charge cycle in Figure 5.6. An atypical increase in current was observed at approximately the 1.25 hr mark, which is likely due to vanadium trapped in tubing or the side walls of the 83 L tanks being remixed with the bulk of the solution. It is expected that increasing the amount of electrolyte or a redesign of the VRFB system (smaller tanks when using 20 L) will assist with reducing the impact of these issues.

5.2.4 SOC-OCV measurements

As mentioned in section 2.2.1, one of the most common SOC monitoring techniques utilized for VRFB systems is via the open-circuit voltage. However, the measurement

of OCV must be done under the condition of zero current, as the use of terminal voltages to monitor SOC would introduce factors such as current dependence and changing temperature, complicating analysis of the results. Hence real-time SOC tracking via OCV requires a separate measurement cell. However, a relationship between OCV and SOC may still be observed by multiple interruptions of the charge/discharge process, during which the current is set to zero.

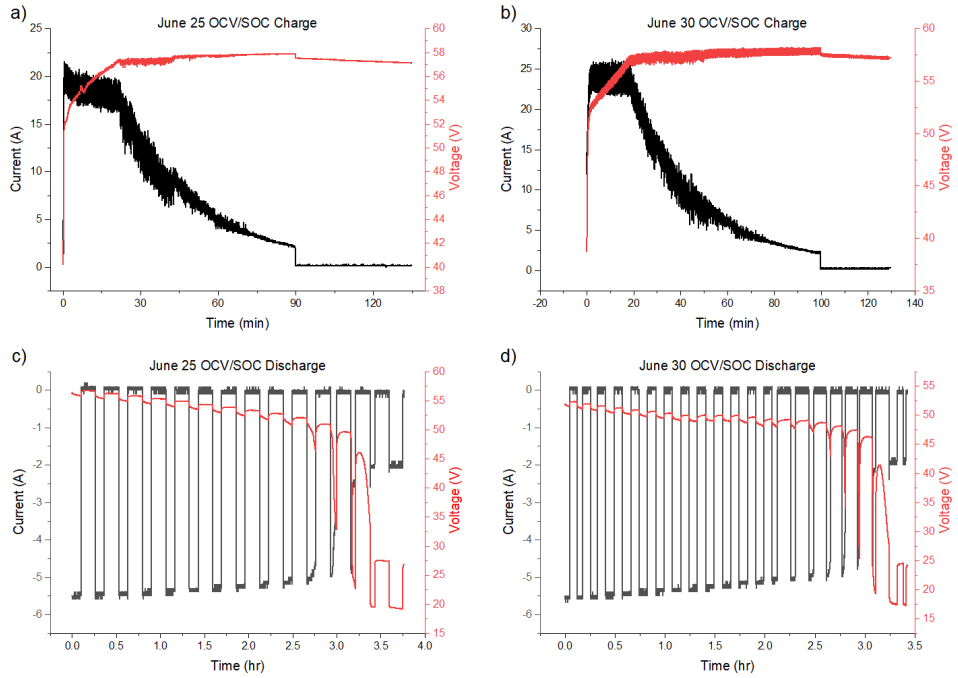

Figure 5.7: VRFB cycling data with big tanks (40 L) and an automatic rebalancing tube during the OCV-SOC test. Charge current/voltage using a) 20A and b) 25 A max charge currents. Discharge current/voltage after using a c) 20A and d) 25 A max charge current.

This concept is utilized to monitor the OCV over the course of the discharge process. To reduce errors generated by the initial charge process, the battery was left to rest at zero current before the first discharge segment was performed. A relaxation period after each discharge segments allows for stabilization of the stack voltage, and quasi-OCV values are obtained from these stabilized values. The experimental

process can be seen schematically in Figure 5.7. Based on observations made from the initial experiments (Figure 5.7 a) and c)), the test was then changed to allow more data points could be obtained at high and low SOCs. These experimental modifications can be seen in Figure 5.7 b) and d). OCV values are acquired via the average (stabilized) voltage of the relaxation periods during the discharge process. OCV results from both experiments are shown in Figure 5.8.

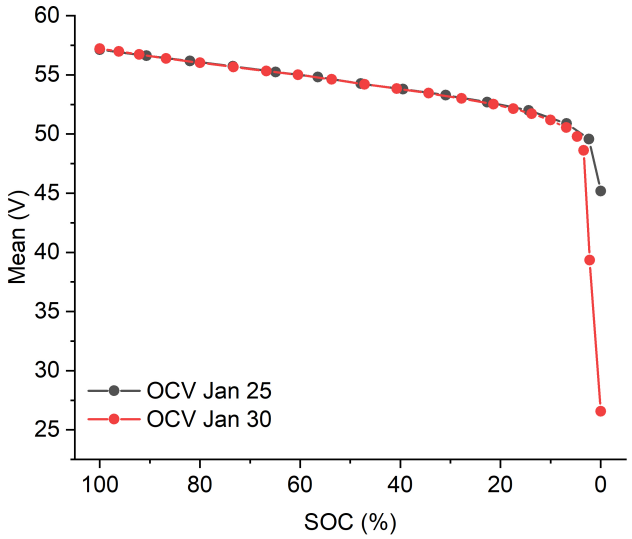

Figure 5.8: Measured OCV after using a 20 A (Jan 25) and 25 A (Jan 30) max charge current

Although the charge current was increased from 20 A to 25 A, it did not have a major effect on the open circuit voltage values obtained throughout the test. As mentioned previously, the electrolyte was charged up to the same 1-2A cutoff point after reaching 62V in both cases, causing them to have the same expected discharge performance. The largest deviations are observed at around 5% SOC, which are caused by the diminishing amounts of V^{2+} and V^{5+} present in the electrolyte. The measured voltage depends on the ratio of V^{3+}/V^{2+} and V^{4+}/V^{5+} present within the stack. These ratios may change over several minutes due to the fact that electrolyte mixing within the electrolyte tanks is not instantaneous upon return from the stack.

These variations lead to a reduction in accuracy during the estimation of SOC. Increasing the electrolyte volume and modification of the electrolyte tanks to promote electrolyte mixing may assist with the mitigation of these issues. The use of a secondary SOC detection cell may also improve accuracy in addition to allowing for real time OCV monitoring. Furthermore, the OCV is currently being measured via the relatively large 40 cell stack with a large electrode area. Because of this, it takes a longer time for electrolyte to be fully 'flushed' from the stack, and hence longer for an accurate voltage reading to be obtained.

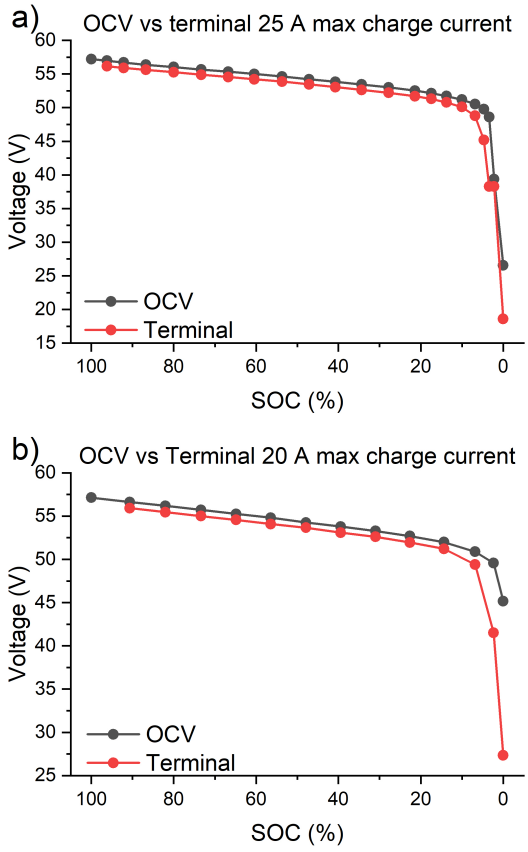

Figure 5.9: OCV vs terminal voltage during a 5.5 A discharge through a 10 ohm resistor after charging at a) 20 A max b) 25 A max

These experiments also allow us to observe the relationship between terminal and open circuit voltages. The previously obtained OCV values are compared to the terminal voltages observed during discharge in Figure 5.9. The current applied dur-

ing the discharge process gives rise to overpotentials which causes the OCV being approximately 0.88 V higher than the terminal voltage.

These results provide a mechanism to estimate the SOC of the VRFB based on the OCV at rest or via the terminal voltage during discharge. However, estimation via terminal voltages will only be valid when the same 5 A discharging current profile is used. And although the experiment modifications allowed more precision to be obtained in the 0-20% and 80-100% SOC regimes, large OCV fluctuations are observed in the low SOC ranges. As such, the estimation of SOC may only be valid above 20% SOC.

5.2.5 Recommended VRFB operation strategies

As the stack has 40 cells, the output voltage during the charge/discharge process is typically restricted to a 40-62 V range as per the Nernst equation. As such, the current and electrolyte volume work in tandem to control the power/capacity ratio. The electrolyte volume plays a major role in determining the most suitable range of input parameters for use during battery operation.

In general, a larger power/capacity ratio decreases the accuracy of battery monitoring due to the decreased cycling time. An example of an unsuitable power/capacity ratio can be seen in Section 5.2.3, where a large discharge current leads to a voltage profile which deviates from that predicted by the Nernst equation. Errors such as this may be reduced via the reduction of the power/capacity ratio, which may be achieved via an increase in electrolyte volume.

Should an increase in electrolyte volume not be feasible, the charging/discharging current may be modified based on observations made from experimental results. In the current experiments, discharging was done under constant resistance, resulting in maximum currents in excess of 5 A and 45 A. For future applications, it is suggested that discharging (as well as charging) be done under constant current. In addition to generating a fixed reaction rate, doing so also allows multiple discharging currents to

be tested (ex 1-50 A in 1 A steps), and an optimal value chosen based on application needs. As high currents decrease the efficiency and may negatively impact stack/-electrolyte health and monitoring, it is suggested that the lowest acceptable current be used.

For experimental consistence, the chosen discharge current may also be used as the maximum current for the charge process. The discharge capacity will also be affected by the maximum voltage and the current at which charging is terminated. While side reactions such as hydrogen and oxygen evolution occur with a faster rate/likelihood at higher voltages, an upper limit of 62 V provided superior results over 58 V, and is suggested for future work. Upon reaching 62 V, the current density gradually decreases ('absorption' mode). Although allowing the current to drop to near zero during this process will result in the best discharge performance, its time requirements are also much larger. Hence while a 0A cutoff is preferable for VRFB performance, it may be modified based on application requirements.

The electrolyte flowrate may then be optimized based on the chosen current. in general, a higher flowrate results in better charge/discharge resistance due to improved kinetics and reduced concentration overpotentials at the electrodes. However, running the pumps for extended periods at high power generally decreases the pump lifetime, and increases the auxilliary power costs. As the output flowrate of the pumps is highly system dependant, it is suggested that multiple flowrates be tested to determine their suitability for long term use.

The VRFB system design may also be optimized based on these parameters and the desired application. Once the electrolyte capacity is chosen based on the charge/discharge currents, the electrolyte reservoirs may be chosen. It is suggested that the smallest possible reservoirs be used in order to both limit air oxidation of V^{2+}, and promote mixing (if there is lots of unutilized reservoir space, electrolyte droplets may cling to the side walls and no longer have the ability to travel the the stack).

For electrolyte rebalancing and the mitigation of symmetric capacity losses, it is

suggested that it be done via a tube connecting the two electrolyte reservoirs. In order to limit self-discharge processes and increase the cycling efficiency, it is suggested that a needle valve be used in only allow electrolyte transfer upon the application of a pressure differential (difference in electrolyte volumes).

5.3 SOC Sensor

The flow cell described in section 4.2 has a sandwich-type structure, which allows for adjustment of the cavity thickness. A larger cavity thickness results in higher absorbance values and a lower magnitude of voltage change due to the increased optical path through the electrolyte. While a smaller cavity thickness typically results in better data acquisition by the photodiode due to increased light transmission through the electrolyte, it also reduces the electrolyte flowrate through the stack due to the flow cell's in-line placement between the pumps and stack inlets.

The charge/discharge process is performed in a similar manner as was done in section 5.2.3, with maximum charging currents of 30 A, and discharging under a constant 1.4 Ω resistance to achieve maximum currents of approximately 45 A. This cycling process may be seen in Figure 5.10 for the case of the negative electrolyte with a $\frac{1}{4}$" optical path through the electrolyte.

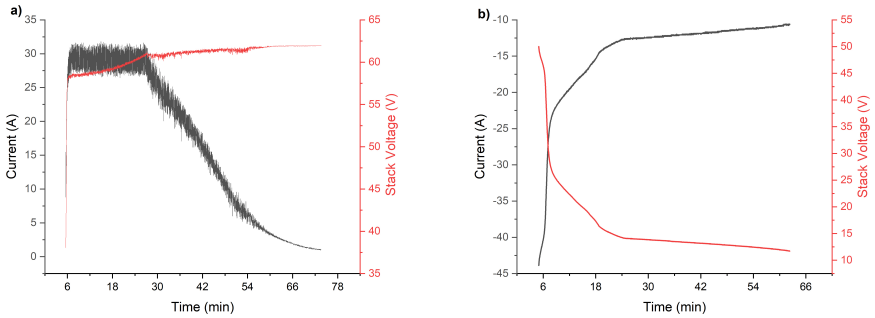

Figure 5.10: Stack data obtained during negative electrolyte absorbance test performed on a 1/14" flow cell. a) 30 A charge process, b) 45 A max discharge process

Three flow cell thicknesses were tested in order to assess their suitability for SOC

detection ($\frac{1}{4}$", $\frac{1}{8}$", $\frac{1}{16}$"). Results from the negative electrolyte are shown in section 5.3.1, while the results from the positive electrolyte are shown in section 5.3.2. All tests were performed utilizing the same charge/discharge process shown in Figure 5.10, a photodiode circuit design such as shown in Figure 4.4, and photodiode placement in a 2" deep plastic tray beneath the flow cell.

The photodiode has a 2 pA dark current, which produces fluctuations on the order of 10^{-9} V, below the 0.03 V resolution of the USB-6211 monitoring system. The 24 V reverse bias results in a reduction of the junction capacitance to 23.6 pF, and a decrease in the rise time to 51.8 ns. The current response from the photodiode (equation 3.12) is monitored under a 100 $k\Omega$ load resistance. The photodiode shows a peak responsivity of 0.6 A/W at 960 nm, and an average responsivity of about 0.32 A/W for wavelengths in the visible range. This results in an expected maximum of 1.7-3 W if all photons from the 550 lumen light source reached the photodiode. However, the light source produces a beam of light with a 30 degree divergence angle, which results in a large spot size after exiting the flow cell. As the photodiode only has a 1.21 mm^2 active area and 92% of the light is transmitted through each of the flow cell's endplates, experimental results from the $\frac{1}{4}$" flow cell only displayed a peak photodiode response of 6.5 V when no electrolyte is present in the cell.

5.3.1 Negative electrolyte

The negative electrolyte was tested with a $\frac{1}{4}$" thick flow cell, the results of which are shown in Figure 5.11. Due to the high absorbance of the electrolyte, a majority of the data was masked due to no light being transmitted through the cell onto the photodiode. Therefore, a reliable relationship between SOC and photodiode voltage could not be formed over the majority of the charge/discharge process.

In order to reduce the absorbance of the electrolyte, the configuration of the flow cell was modified such that the optical path through the electrolyte was reduced to $\frac{1}{8}$". Data from this flow cell configuration is shown in Figure 5.12.

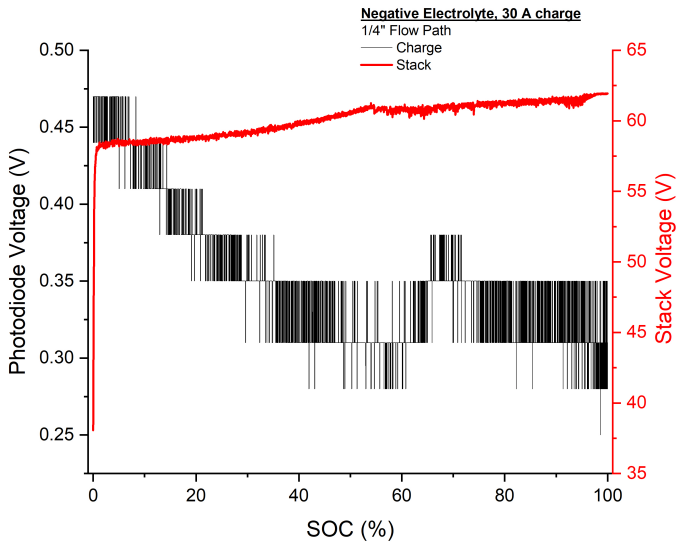

Figure 5.11: Negative electrolyte absorbance test utilizing a 1/4" flow cell (30 A charge)

Although results obtained from this configuration are much better that previously obtained with the $\frac{1}{4}$" configuration, the electrolyte becomes too dark at approximately 50% SOC, after which no light is transmitted to the photodiode. In order to decrease the electrolyte absorbance, the flow cell thickness is further reduced to $\frac{1}{16}$", the data from which is shown in Figure 5.13.

As this was the thinnest tested configuration, it provided the best data coverage, with small amounts of light being transmitted at all SOCs. However, an adequate relationship between SOC and electrolyte absorbance could not be determined due to a poor voltage response from the photodiode. In order to obtain a better voltage response from the photodiode, the circuit may be redesigned such to include an operational amplifier. One possible design is shown in Figure 4.5. Although this configuration was not tested, better results are expected due to light transmission through the cell at all SOCs and the amplifier providing a voltage gain of about 16. Additionally, the 2" deep plastic tray may be replaced with the housing shown in Figure 4.6 to allow near direct contact with the flow cell endplate. This is expected to reduce beam divergence by approximately 700 mm^2, increasing the amount of

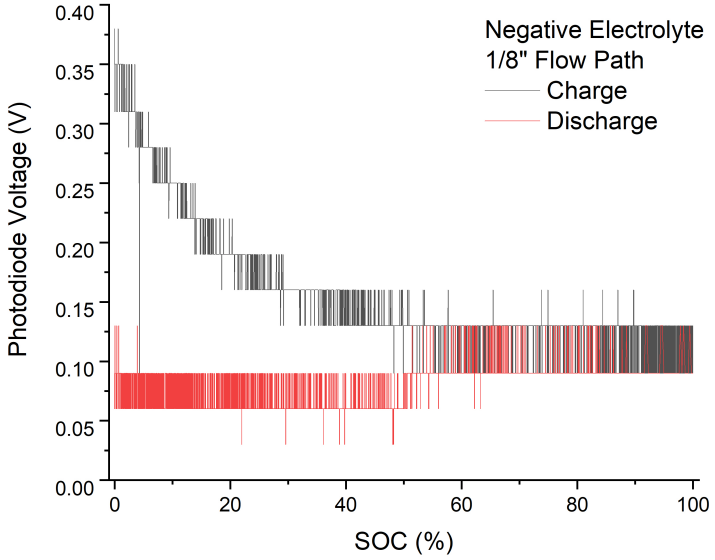

Figure 5.12: Negative electrolyte absorbance test utilizing a 1/8" flow cell (30 A charge)

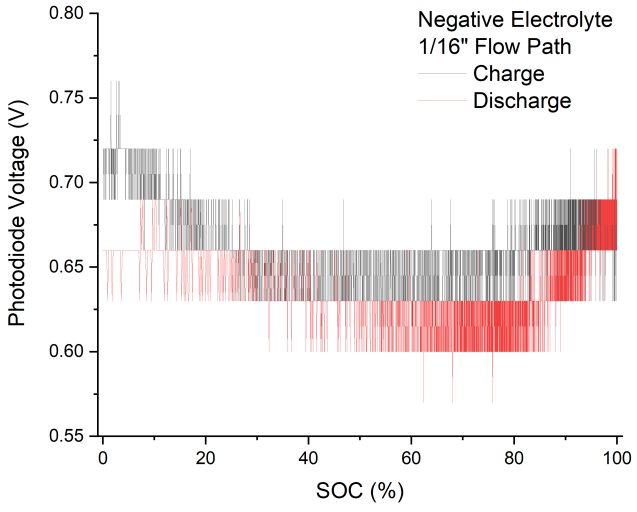

Figure 5.13: Negative electrolyte absorbance test utilizing a 1/16" flow cell (30 A charge)

transmitted light which falls on the detector. A similar effect may be achieved via utilization of a higher intensity light source with less beam divergence.

5.3.2 Positive Electrolyte

The positive electrolyte changes from blue to yellow upon charging, resulting in high transmittance at low and high SOC values. However, the electrolyte displays a non-linear SOC-absorbance relationship, due to V^{4+}/V^{5+} complexing at mid-SOC values. The consequences of this can be seen in Figure 5.14, where high absorbance was observed in the 20-90% SOC ranges. At low and high SOCs, a very large voltage response was observed compared to the negative electrolyte due to the brightness of the electrolyte at these extremes (blue/yellow vs violet/green). However, V^{4+}/V^{5+} complexing at mid SOC values results in a very dark, almost black electrolyte which absorbs light in excess of Beer-Lambert's Law.

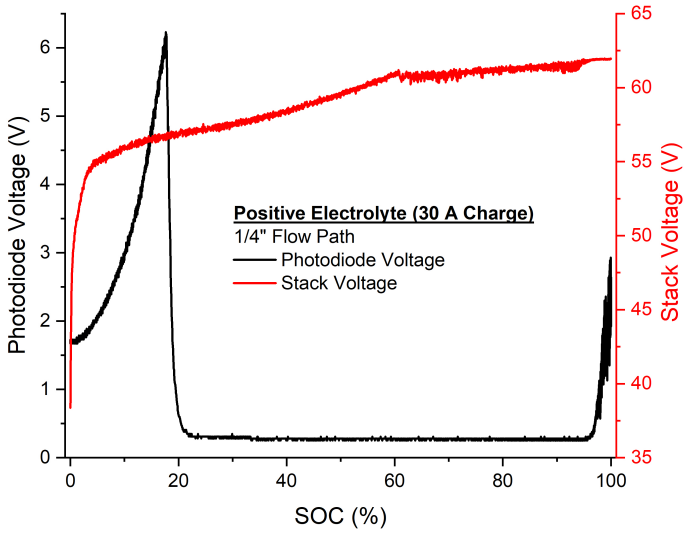

Figure 5.14: Positive electrolyte absorbance test utilizing a 30 A charge and 1/4" optical path (charge process)

As with testing of the $\frac{1}{4}$" flow cell on the negative electrolyte, no light was observed to be transmitted through the flow cell onto the photodiode in the mid-SOC range

(20-80%). The absorbance at these SOCs is much higher than that observed in the negative electrolyte, and improvements were not seen when reducing the optical path to $\frac{1}{8}$" or $\frac{1}{16}$". Due to the lack of light transmission at all SOC values, an operational amplifier alone will not be sufficient for data improvement - a thinner flow cell or stronger light source is required. However, further reduction in flow cell thickness to $\frac{1}{50}$" resulted in a pressure drop that the pumps were unable to overcome. In order to overcome this, future experiments may benefit from the utilization of a wedge shape flow cell design such that the optical path may be reduced with a lower pressure drop.

Due to the high discharge current (and resultant short discharge times) used during testing, poor accuracy was observed during measurement of the negative electrolyte's discharge cycle. Due to the positive electrolyte displaying a much higher magnitude of voltage response compared to the negative electrolyte, this can be easily seen in Figure 5.15.

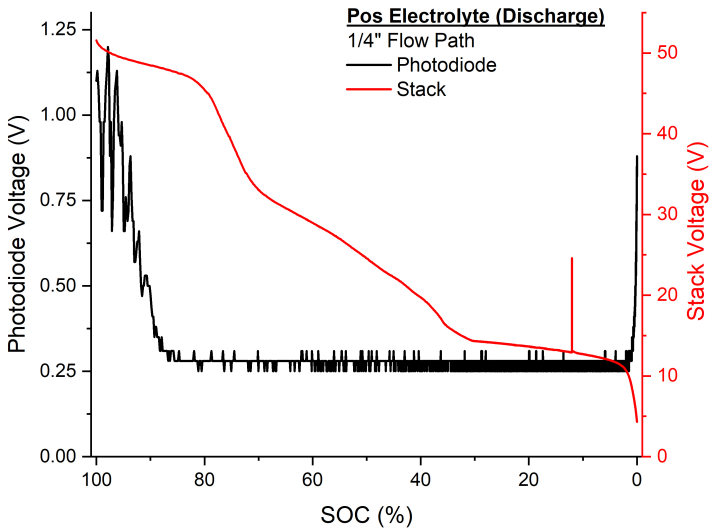

Figure 5.15: Positive electrolyte absorbance test utilizing a 30 A charge and 1/4" optical path (discharge process)

While the charge process displayed photodiode responses in excess of 6 V at low SOCs (Figure 5.14), only a 1.25 V peak voltage response was observed during the

discharge process. In order to prevent this from occurring, future tests should employ a lower cycling currents and/or an increase in electrolyte volume. This increases the charge/discharging time, both increasing the number of data points retrieved and decreasing the potential for errors caused by incomplete mixing of electrolytes within the electrolyte reservoirs etc.

5.3.3 SOC sensor summary and applicability

Due to the high absorbance of the positive electrolyte, this sensing method may be better suited for the acquisition of the negative electrolyte's SOC. However, absorbance sensing of the positive electrolyte may be done via the use of an adequately thin layer of electrolyte, which is easily configurable with the sandwich-type structure of the flow cell, or a stronger light source with less beam divergence. This allows monitoring of both electrolytes to be performed simultaneously, which is ideal as it allows asymmetric losses to be detected and accounted for.

Due to practical limitations, the interior thickness of current design is limited to $\frac{1}{16}$" because of the chosen pump. Hence to obtain measurements from the positive electrolyte over the full SOC range, the size of the flow cell may need to be reduced to a point where a secondary pump is required. Design alterations of the flow cell may also assist with measurement of the positive electrolyte without the use of a secondary pump. A wedge-shaped design may be more suitable for the reduction of the electrolyte's optical path, while minimizing the pressure drop through the cell. However, uniform electrolyte distribution within the cell may be negatively impacted when utilizing this approach, potentially leading to a decrease in SOC detection accuracy. As such, testing would need to be performed in order to ensure that proper electrolyte flow is observed and dead zones are not present within the cell.

As an alternative to redesign of the flow cell, the 550 lumen light source may be replaced with stronger light source. The use of a strong enough light source will ensure that light transmission is observed at all SOCs. Combined with the integration of an

operational amplifier into the photodiode circuit (Figure 4.5), and the utilization of a housing such as the one seen in Figure 4.6 to eliminate the 2" between the flow cell and detector, photodiode voltages may be obtained with sufficient precision to allow for SOC monitoring of both electrolytes without reduction of the flow cell thickness below 1/16".

In addition to its high absorbance at mid-range SOCs, another drawback of utilizing the positive electrolyte for SOC detection is that it displays a parabolic relationship between absorbance and SOC. As such, a single photodiode voltage is indicative of two possible SOCs. However, if both electrolytes are being monitored simultaneously, this ambiguity can be removed via comparison with the negative electrolyte.

Chapter 6

Conclusions, Recommendations, & Future Work

6.1 Conclusions

Testing was performed on a 2.5 kW VRFB stack with 8L and 40 L volumes of electrolyte. The VRFB electrolyte is prone to several degradation mechanisms which reduces its capacity over time. In order to mitigate these issues and extend the lifetime of the electrolyte, a suitable method of SOC detection is required. While simple SOC monitoring is commonly done via voltage, this is only able to detect symmetrical capacity losses across the full system.

Symmetrical capacity losses may be mitigated via simple remixing of the positive and negative electrolytes. An automatic electrolyte re-balancing mechanism may be constructed by adding a hydraulic shunt between the two tanks. This gives the VRFB system the ability to automatically regulate volume differences between the reservoirs and mitigate capacity loss due to bulk electrolyte transfer through the membrane during the charge/discharge process. This concept was tested and successfully demonstrated the ability to recover capacity loss due to net water transport (section 5.1.2).

A light sensor (photodiode or CCD) may be used for the monitoring of each individual electrolyte in order to track unsymmetrical capacity loss between the two tanks. An SOC sensor based off of a white light source may be the most simple, scalable,

and economical choice for commercial applications. As such, a FD11a photodiode was used to track the absorbance of a white light source through a thin volume of electrolyte ($\frac{1}{4}$", $\frac{1}{8}$", $\frac{1}{16}$" optical paths) during the charge/discharge process. This is achieved via the creation of a flow cell with clear acrylic sheets such that approximately 84.64% of the 550 lumen light source's (visible) light can be expected to be transmitted through the flow cell when no electrolyte is present (92% transmission through each endplate).

These experiments were unsuccessful in monitoring SOC for both the positive and negative electrolytes due to the high absorbance of the electrolyte. In order to improve results while utilizing the current 550 lumen light source, further reduction of the flow cell thickness is required in order to decrease the optical path and increase light transmission through the electrolyte. As an alternative, a brighter light source may be used for illumination of the electrolyte. These options should allow data coverage to be obtained for all SOCs, while a voltage gain may be created through the use of an operational amplifier in the photodiode circuit. Similar gains may also be achieved via redesign of the photodiode housing to eliminate the 2" distance between the flow cell and detector.

6.2 Future Work

The thickness of the flow cell cavity dictates the optical path through the electrolyte, with larger optical paths resulting in higher absorbance values. Smaller optical paths are desired due to the high absorbance of the electrolyte, which may cause data to be 'masked' over the full SOC range at larger optical paths (as was seen in 5.3). However, reducing the flow cell thickness causes a larger pressure drop through the cell, and pump properties may impose a lower limit to the thickness' achievable in practice. The high absorbance of the positive electrolyte places constraints on the design of the SOC sensor/VRFB system. The use of a secondary pump may assist with the operation of thinner SOC flow cell configurations, while a wedge-shaped flow

cell design may be used in order to reduce the absorbance while continuing to use the flow cell inline with the current pump system.

As mentioned previously, pump properties may limit the practically achievable flow cell thicknesses. The shape of the electrolyte's flow path within the cell may be optimized such that the pressure drop within the cell is minimized. This can be achieved by changing the shape of the flow cell's hollow interior gasket(s). This may be done in tandem with optimization of the flow cell size. While the current flow cell configuration has a 6" x 6" area, the photodiode only has a 1.2 mm^2. As such, the size of this cell may be reduced based on sensor, strength, and flow property requirements.

Future studies should be done on the effect of temperature to ensure additional calibration is not required to accurately correlate the SOC with data obtained from the photodiode due to shifts in electrolyte absorption at extreme temperatures. All future testing should be done utilizing lower power/capacity ratios. This is expected to provide more stability and repeat-ability between tests. Further accuracy improvements may be generated via the integration of an operational amplifier into the photodiode PCB, and by reducing/eliminating the space between the photodiode and flow cell.

Bibliography

[1] S. Montzka, E. Dlugokencky, and J. Butler, "Non-co2 greenhouse gases and climate change," *Nature*, vol. 476, pp. 43–50, 2011. DOI: https://doi.org/10.1038/nature10322.

[2] A. Schavan, *Germany's energy research plan*, Oct. 1900. [Online]. Available: https://science.sciencemag.org/content/330/6002/295.

[3] M Anvari, G Lohmann, M Wächter, P Milan, E Lorenz, D Heinemann, M. R. R. Tabar, and J. Peinke, "Short term fluctuations of wind and solar power systems," *New Journal of Physics*, vol. 18, no. 6, p. 063 027, Jun. 2016. DOI: 10.1088/1367-2630/18/6/063027.

[4] N. R. Canada, *Renewable energy facts*, Oct. 2019. [Online]. Available: https://www.nrcan.gc.ca/science-data/data-analysis/energy-data-analysis/energy-facts/renewableenergy-facts/20069.

[5] B. Livingston, "The alberta electrical grid: What to expect in the next few years in alberta," *The School of Public Policy*, vol. 11, Apr. 2018. DOI: https://doi.org/10.11575/sppp.v11i0.43162.

[6] N. R. Canada, *Residential ghg emissions by energy source and end use*, 2019. [Online]. Available: http://oee.nrcan.gc.ca/corporate/statistics/neud/dpa/showTable.cfm?type=HB&sector=res&juris=00&rn=6&page=4&CFID=6558177&CFTOKEN=cbf2e34ea5062460-223E9DA9-BCAA-1A35-CCFC281D38E83DE1.

[7] K. M. Tan, V. K. Ramachandaramurthy, J. Y. Yong, S. Padmanaban, L. Mihet-Popa, and F. Blaabjerg, "Minimization of load variance in power grids—investigation on optimal vehicle-to-grid scheduling," *Energies*, vol. 10, no. 11, p. 1880, 2017. DOI: 10.3390/en10111880.

[8] I. E. Agency, "Global ev outlook 2016," 2016. DOI: 10.1787/9789264279469-en.

[9] T. Mohammadi and M. Skyllas-Kazacos, "Preparation of sulfonated composite membrane for vanadium redox flow battery applications," *Journal of Membrane Science*, vol. 107, no. 1, pp. 35–45, 1995, ISSN: 0376-7388. DOI: https://doi.org/10.1016/0376-7388(95)00096-U. [Online]. Available: https://www.sciencedirect.com/science/article/pii/037673889500096U.

[10] K. Ngamsai and A. Arpornwichanop, "Measuring the state of charge of the electrolyte solution in a vanadium redox flow battery using a four-pole cell device," *Journal of Power Sources*, vol. 298, pp. 150–157, 2015, ISSN: 0378-7753. DOI: https://doi.org/10.1016/j.jpowsour.2015.08.026. [Online]. Available: https://www.sciencedirect.com/science/article/pii/S0378775315301804.

[11] A. Bhattarai, P. C. Ghimire, A. Whitehead, R. Schweiss, G. G. Scherer, N. Wai, and H. H. Hng, "Novel approaches for solving the capacity fade problem during operation of a vanadium redox flow battery," *Batteries*, vol. 4, no. 4, 2018, ISSN: 2313-0105. DOI: 10.3390/batteries4040048. [Online]. Available: https://www.mdpi.com/2313-0105/4/4/48.

[12] Z. Tang, D. Aaron, A. Papandrew, and T. Zawodzinski, "Monitoring the state of charge of operating vanadium redox flow batteries," *ECS Transactions*, vol. 41, no. 23, pp. 1–9, 2012. DOI: http://dx.doi.org/10.1149/1.3697449.

[13] M. Skyllas-Kazacos and M. Kazacos, "State of charge monitoring methods for vanadium redox flow battery control," *Journal of Power Sources*, vol. 196, pp. 8822–8827, 20 2011. DOI: 10.1016/j.jpowsour.2011.06.080.

[14] K. Shin, C. Jin, J. So, S. Park, D. Kim, and S. Yeon, "Real-time monitoring of the state of charge (soc) in vanadium redox-flow batteries using uv–vis spectroscopy in operando mode," *Journal of Energy Storage*, vol. 27, 101066 2020. DOI: 10.1016/j.est.2019.101066.

[15] G. J. May, A. Davidson, and B. Monahov, "Lead batteries for utility energy storage: A review," *Journal of Energy Storage*, vol. 15, pp. 145–157, 2018. DOI: https://doi.org/10.1016/j.est.2017.11.008.

[16] S. Dhameja, *Electric vehicle battery systems*. Elsevier Inc., 2002, ISBN: 978-0-7506-9916-7. DOI: https://doi.org/10.1016/B978-0-7506-9916-7.X5000-6.

[17] P. Du and N. Lu, *Energy Storage for Smart Grids: Planning and Operation for Renewable and Variable Energy Resources (VERs)*. Elsevier Inc., 2014, ISBN: 978-0-12-410491-4. DOI: https://doi.org/10.1016/C2012-0-06954-2.

[18] K. Lourenssen, J. Williams, F. Ahmadpour, R. Clemmer, and S. Tasnim, "Vanadium redox flow batteries: A comprehensive review," *Journal of Energy Storage*, vol. 25, p. 100 844, 2019. DOI: 10.1016/j.est.2019.100844.

[19] F. Henn, C. Rouvet, A. D. Guibert, and P. Marteau, "Hydrogen and oxygen evolution in sealed lead/acid 2 v cells. in situ gas measurement by raman spectroscopy," *Journal of Power Sources*, vol. 63, pp. 235–246, 2 1996. DOI: 10.1016/s0378-7753(96)02480-9.

[20] A. Hollenkamp, K. Constanti, A. Huey, M. Koop, and L. Aputeanu, "Premature capacity-loss mechanisms in lead/acid batteries," *Journal of Power Sources*, vol. 40, pp. 125–136, 1992. DOI: 10.1016/0378-7753(92)80044-c.

[21] B. University, *Bu-304a: Safety concerns with li-ion*, Apr. 2019. [Online]. Available: https://batteryuniversity.com/learn/article/safety_concerns_with_li_ion.

[22] P. Breeze, "Power system energy storage technologies," in. Dec. 2014, pp. 195–221, ISBN: 9780080983301. DOI: 10.1016/B978-0-08-098330-1.00010-7.

[23] A. Vassallo, "Chapter 17 - applications of batteries for grid-scale energy storage," in *Advances in Batteries for Medium and Large-Scale Energy Storage*, ser. Woodhead Publishing Series in Energy, C. Menictas, M. Skyllas-Kazacos, and T. M. Lim, Eds., Woodhead Publishing, 2015, pp. 587 –607, ISBN: 978-1-78242-013-2. DOI: https://doi.org/10.1016/B978-1-78242-013-2.00017-0. [Online]. Available: http://www.sciencedirect.com/science/article/pii/B9781782420132000170.

[24] Z. Wen, J. Cao, Z. Gu, X. Xu, F. Zhang, and Z. Lin, "Research on sodium sulfur battery for energy storage," *Solid State Ionics*, vol. 179, pp. 1697 –1701, 27 2008. DOI: https://doi.org/10.1016/j.ssi.2008.01.070.

[25] X. Xu, D. Zhou, X. Qin, K. Lin, F. Kang, B. Li, D. Shanmukaraj, T. Rojo, M. Armand, and G. Wang, "A room-temperature sodium–sulfur battery with high capacity and stable cycling performance," *Nature Communications*, vol. 9, 3870 2018. DOI: https://doi.org/10.1038/s41467-018-06443-3.

[26] J. L. Sudworth and A. R. Tilley, *The sodium sulfur battery*. Chapman and Hall Ltd., Jan. 1985.

[27] M. Daghi, M. Sedghi, A. Ahmadian, and M. Aliakbar-Golkar, "Factor analysis based optimal storage planning in active distribution network considering different battery technologies," *Applied Energy*, vol. 183, pp. 456–469, 2016. DOI: 10.1016/j.apenergy.2016.08.190.

[28] A. G. Morachevskii and A. I. Demidov, "Sodium–sulfur system: Phase diagram, thermodynamic properties, electrochemical studies, and use in chemical current sources in the molten and solid states," *Russian Journal of Applied Chemistry*, vol. 90, pp. 661–675, 5 2017. DOI: 10.1134/s1070427217050019.

[29] J. Sangster and A. D. Pelton, "The na-s (sodium-sulfur) system," *Journal of Phase Equilibria*, vol. 18, pp. 89–96, 1 1997. DOI: 10.1007/bf02646762.

[30] *Vanadium sulphate electrolytic solution specification sheet*, Jan. 2021. [Online]. Available: http://www.oxkem.com/product_pdfs/Vanadium\%20electrolyte.pdf.

[31] T. Jirabovornwisut and A. Arpornwichanop, "A review on the electrolyte imbalance in vanadium redox flow batteries," *International Journal of Hydrogen Energy*, vol. 44, pp. 24485 –24 509, 45 2019. DOI: https://doi.org/10.1016/j.ijhydene.2019.07.106.

[32] J. L. Barton and F. R. Brushett, "A one-dimensional stack model for redox flow battery analysis and operation," *Batteries*, vol. 5, no. 1, 2019. DOI: 10.3390/batteries5010025. [Online]. Available: https://www.mdpi.com/2313-0105/5/1/25.

[33] N. Roznyatovskaya, J. Noack, H. Mild, M. Fühl, P. Fischer, K. Pinkwart, J. Tübke, and M. Skyllas-Kazacos, "Vanadium electrolyte for all-vanadium redox-flow batteries: The effect of the counter ion," *Batteries*, vol. 5, no. 1, 13 2019. DOI: https://doi.org/10.3390/batteries5010013. [Online]. Available: https://www.mdpi.com/2313-0105/5/1/13.

[34] I. Technical Glass Products, *Fused quartz transmittance curves*, 2020. [Online]. Available: https://technicalglass.com/fused_quartz_transmission/.

[35] *Spectrophotometry*, Apr. 2019. [Online]. Available: https://www.nist.gov/programs-projects/spectrophotometry.

[36] *Sec2000 - spectrometer*, Apr. 2020. [Online]. Available: https://www.als-japan.com/1352.html.

[37] Lumen, *Photon energies and the electromagnetic spectrum*. [Online]. Available: https://courses.lumenlearning.com/physics/chapter/29-3-photon-energies-and-the-electromagnetic-spectrum/#:~:text=E%3Dhf%3Dhc,10%E2%88%9215%20eV%20%C2%B7%20s..

[38] I. Thorlabs, *Gratings tutorial*. [Online]. Available: https://www.thorlabs.com/newgrouppage9.cfm?objectgroup_id=25.

[39] R. Nave, *Diffraction grating*, Dec. 2020. [Online]. Available: http://hyperphysics.phy-astr.gsu.edu/hbase/phyopt/gratcal.html.

[40] H. Perkampus, *UV-VIS Spectroscopy and Its Applications*. 1992, ISBN: 978-3-642-77479-9. DOI: 10.1007/978-3-642-77477-5.

[41] L. Liu, J. Xi, Z. Wu, W. Zhang, H. Zhou, W. Li, and X. Qiu, "State of charge monitoring for vanadium redox flow batteries by the transmission spectra of v(iv)/v(v) electrolytes," *Journal of Applied Electrochemistry*, vol. 42, pp. 1025–1031, 12 2012. DOI: 10.1007/s10800-012-0477-2.

[42] A. Technologies., *Photodiode theory of operation*, Oct. 2020. [Online]. Available: https://www.aptechnologies.co.uk/support/SiPDs/operation.

[43] B. G. Streetman and S. K. Banerjee, *Solid state electronic devices*. Pearson, 2016. [Online]. Available: http://search.ebscohost.com/login.aspx?direct=true&scope=site&db=nlebk&db=nlabk&AN=1419255.

[44] A. Kay, "Chapter 10 - photodiode amplifier noise," in *Operational Amplifier Noise*. Newnes, 2012, pp. 169–187, ISBN: 9780750685252. DOI: https://doi.org/10.1016/B978-0-7506-8525-2.00010-1. [Online]. Available: http://www.sciencedirect.com/science/article/pii/B9780750685252000101.

[45] Chegg.com, *Definition of junction capacitance*, Oct. 2020. [Online]. Available: https://www.chegg.com/homework-help/definitions/junction-capacitance-4.

[46] E. Tutorials, *Pn junction theory for semiconductor diodes*, Jan. 2018. [Online]. Available: https://www.electronics-tutorials.ws/diode/diode_2.html.

[47] O. Optoelectronics, "Photodiode characteristics and applications," Tech. Rep. [Online]. Available: http://www.osioptoelectronics.com/application-notes/an-photodiode-parameters-characteristics.pdf.

[48] V. Mackowiak, J. Peupelmann, Y. Ma, and A. Gorges, *Nep - net equivalent power*, Oct. 2020. [Online]. Available: https://www.thorlabs.com/images/TabImages/Noise_Equivalent_Power_White_Paper.pdf.

[49] G. Houghton, *Digital camera sensor technology - part 3 ccd sensors explained*, Feb. 2014. [Online]. Available: https://www.youtube.com/watch?v=Xkput-1xNYE.

[50] I. Thorlabs, *Fd11a si photodiode, 400 ns rise time, 320 - 1100 nm, 1.1 mm x 1.1 mm active area*, Jun. 2012. [Online]. Available: https://www.thorlabs.com/thorproduct.cfm?partnumber=FD11A.

[51] Amazon, *Yungui diy prototyping pcb boards, 15pcs 7x10cm single sided bakelite copper clad pcb laminate circuit board*, 2020. [Online]. Available: https://www.amazon.ca/dp/B07TWHLMVP/ref=cm_sw_r_oth_api_fabt1_NyvXFbK2FTZKB.

[52] Amazon, *Tnisesm/60pcs 2 pin & 3 pin 5mm/0.2inch pitch pcb mount screw terminal block connector (can be spliced) tn-t03g*, 2020. [Online]. Available: https://www.amazon.com/Tnisesm-0-2inch-Terminal-Connector-Spliced/dp/B088LSS14J/ref=sr_1_34?dchild=1&qid=1606767789&s=industrial&sr=1-34.

[53] E. Components, *Lm741 - general purpose op-amp*, 2020. [Online]. Available: https://www.electroncomponents.com/LM741-Op-Amp.

Appendix A: Cost

This appendix contains compiled information regarding the costs associated with construction and operation of the VRFB system. This including safety equipment, VRFB system components, SOC sensor components, and other electrical equipment.

A.1 SOC sensor costs

The main components of the SOC sensor are the flow cell and the photodiode circuit/-light source. Lists of costs for each component is found in Table A.1. All items were purchased from McMaster-Carr with the exception of the photodiode (thorlabs), circuit boards (YUNGUI), screw terminals (Tnisesm), and operational amplifier (Electron Components).

Table A.1: VRFB SOC sensor costs

Flow Cell						
Part Type	Part Name	Product code	Cost		Description	source
			Per Pack	Total		
Acrylic Sheets	Clear Scratch- and UV-Resistant Cast Acrylic Sheet, 6" x 6" x 1/2"	8560K274	$8.97	$17.94	Top endplate (1/2")	McMaster-Carr
	Clear High-Strength UV-Resistant Acrylic, 6" x 6" x 1/16"	4615T61	$1.61	$1.61	Bottom endplate (1/16")	McMaster-Carr
	Clear High-Strength UV-Resistant Acrylic, 6" x 6" x 1/8"	4615T91	$2.39	$2.39	Bottom endplate (1/8")	McMaster-Carr
Gaskets	Gasket Material, High-Temperature Silicone Strip, 6" Wide x 36" Long x 1/16" Thick	8525T577	$24.00	$24.00	describe	McMaster-Carr
	High-Temperature Silicone Rubber Sheet, Ultra-Thin, 6" x 6", 0.020" Thick, 20A Durometer	86435K15	$14.20	$28.40	describe	McMaster-Carr
	High-Temperature Silicone Rubber Sheet, Ultra-Thin, 6" x 6", 0.010" Thick, 20A Durometer	86435K121	$11.46	$22.92	describe	McMaster-Carr
Connections	Super-Flow Barbed Fitting for Food and Beverage, Straight Adapter for 1/2" Tube ID x 1/2 NPT Male, packs of 10	2808K36	$8.68	$8.68	describe	McMaster-Carr
	Medium-Strength Grade 5 Steel Hex Head Screw, Black Ultra-Corrosion-Resistant Coated, 1/4"-20 Thread, 2" Long, packs of 5	94967A412	$8.10	$16.20	describe	McMaster-Carr
	Grade 8 Steel Washer, Black Ultra-Corrosion-Resistant, 1/4" Screw Size, 0.75" OD, packs of 10	98026A111	$6.93	$6.93	describe	McMaster-Carr
	Medium-Strength Steel Hex Nuts - Grade 5, Black Ultra-Corrosion-Resistant Coated, 1/4"-20 Thread Size, packs of 10	98797A029	$5.93	$5.93	describe	McMaster-Carr
Photodiode Circuit						
Main Components	Duracell 550 Lumen 3-pack Headlamp	1600263	$26.99	$26.99	Light source	McMaster-Carr
	Si Photodiode, 400 ns Rise Time, 320 - 1100 nm, 1.1 mm x 1.1 mm Active Area	FD11A	$14.58	$14.58	Photodiode	Thorlabs, Inc. [50]
	YUNGUI DIY Prototyping PCB Boards,15Pcs 7x10cm Single Sided Bakelite Copper Clad PCB Laminate Circuit Board	B07TWHLMVP	$16.99	$16.99	1.5 mm thick PCB Board	YUNGUI (Amazon) [51]
	Tnisesm/60pcs 2 Pin & 3 Pin 5mm/0.2inch Pitch PCB Mount Screw Terminal Block Connector (Can be Spliced) TN-T03G	B088LSS14J	$8.99	$8.99	PCB Screw terminals	Tnisesm (Amazon) [52]
Other Items	Resistors, Carbon Film, 0.022" Wire Diameter, 100 Ohms Resistance (5 pack)	1348N204	$2	$2	100 Ohm Resistor	McMaster-Carr
	Resistors, Carbon Film, 0.022" Wire Diameter, 220 Ohms Resistance (5 pack)	1348N213	$2	$2	220 Ohm Resistor	McMaster-Carr
	Resistors, Carbon Film, 0.022" Wire Diameter, 330 Ohms Resistance (5 pack)	1348N218	$2	$2	330 Ohm Resistor	McMaster-Carr
	Resistors, Carbon Film, 0.022" Wire Diameter, 1 kilohms Resistance (5 pack)	1348N205	$2	$2	1000 Ohm Resistor	McMaster-Carr
	Resistors, Carbon Film, 0.022" Wire Diameter, 5.1 kilohms Resistance (5 pack)	1348N231	$2	$2	5100 Ohm Resistor	McMaster-Carr
	Aluminum Electrolytic Capacitors, 100 µ-F Capacitance, 35V DC (5 pack)	5077N18	$4	$4	100 µF Capacitor	McMaster-Carr
	LM741 - General Purpose Op-Amp	ICOA_LM741	$0.24	$0.24	Operational amplifier	Electron Components [53]

A.2 VRFB system costs

Costs for remaining VRFB system components are found in Tables A.2 and A.3. This includes the mechanical components required for the VRFB frame, the electrolyte tanks, tubing and fittings, VRFB electrolyte, safety equipment, pumps, flowmeters, and other electronics.

Additional costs not included on the table are the:

1) Multifunctional I/O device (USB-6211) obtained from National Instruments, $1485 CAD

2) Bidirectional inverter/charger (MultiPlus-II 48/5000/70-50) obtained from Victron Energy, $2100 CAD

3) 40 cell, 50 A (nominal), 2.5 kW Stack obtained from Volterion, $3000 CAD

Table A.2: VRFB System Costs Part 1

Main Components						
	Part Type	Part Name & Description	Supplier	Product code	Quantity	Cost (USD)
Frame Components	T-Slotted Framing Quad Rail, Silver, 2" High x 2" Wide, Solid, 6 ft.	6 foot Rail	McMaster-Carr	47065T501	10	$534.3
	T-Slotted Framing Quad Rail, Silver, 2" High x 2" Wide, Solid, 2 ft.	2 foot Rail	McMaster-Carr	47065T501	17	$329.46
	Snap on End Cap for 2" High Quad Rail T-Slotted Framing	Vertical rail caps	McMaster-Carr	47065T982	4	$13.96
	T-Slotted Framing Silver Diagonal Brace for 2" High Double/Quad Rail, 6" Long	Diagonal Brace	McMaster-Carr	47065T187	8	$123.60
	T-Slotted Framing Silver Corner Bracket, 1" Long for 2" High Double/Quad Rail	Corner Bracket	McMaster-Carr	47065T237	48	$365.76
	L-Shaped Connector for 1" High Single Rail T-Slotted Framing	L-Connector	McMaster-Carr	5537T315	32	$80
	Polycarbonate Solid Panel, 2 Feet x 2 Feet for T-Slotted Framing	Panels for middle platform	McMaster-Carr	47065T325	2	$104.3
Main Tanks	Vertical Plastic Tank with Drain 22 Gallon Capacity	22 gal. (83 L) Tanks	McMaster-Carr	3662K33	2	$586.44
	Dark Gray PVC Y-Strainer with 3/4 NPT Connection and PVC Plastic Screen, 1/32"	Strainer	McMaster-Carr	4425K32	2	$160.08
	Mesh Screen for 3/4 Pipe Size PVC Y-Strainer, 40 Mesh Size	Strainer replacement mesh	McMaster-Carr	44915K12	2	$62.32
	Thick-Wall Polypropylene Pipe Fitting for Chemicals Plug with External Hex Drive Style, 3/4 NPT Male	Main Tank Plugs	McMaster-Carr	46885K213	2	$5.90
	Thick-Wall Polypropylene Pipe Fitting for Chemicals, Bushing Reducing Adapter, 2 NPT Male x 3/4 NPT Female	Tank Return line adaptor	McMaster-Carr	46885K268	2	$8.62
Startup Cylinders	Impact-Resistant Polycarbonate Round Tube 6" OD, 5-3/4" ID, Clear, 1 ft.	Startup cyilnder	McMaster-Carr	8585K58	2	$81.06
	Clear Acrylic Disc, 1/4" Long, 7" Diameter	Cap for startup cylinder	McMaster-Carr	8581K38	4	$67.76
	Thick-Wall Through-Wall Pipe Fitting Threaded PVC, for Water, 3/4 NPT, 2-7/8" Long	Bulkhead fitting for startup cylinder	McMaster-Carr	36895K162	4	$87.28
	Structural Adhesive Chemically-Resistant Epoxy, Lord 204/19, 1.69 oz. Cartridge	Adhesive for startup cylinder	McMaster-Carr	66195A15	2	$33.16
Barbed fittings	Super-Flow Barbed Fitting for Food and Beverage Plastic Adapter, for 1/2" Tube ID x 3/4 NPT Male	Barbed fittings for 1/2" tubing (pack of 10)	McMaster-Carr	2808K42	5	$8.21
	Chemical-Resistant Barbed Tube Fitting for 1/2" Tube ID x 1/4 NPT Male, 150°F Maximum	Flowmeter barbed fittings (pack of 10)	McMaster-Carr	53415K212	1	$9.47
	Super-Flow Barbed Fitting for Food and Beverage Plastic Adapter, for 3/4" Tube ID x 3/4 NPT Male	Barbed fittings for 3/4" stack tubing (pack of 10)	McMaster-Carr	2808K44	4	$8.48
	Chemical-Resistant Barbed Tube Fitting for 3/32" Tube ID x 1/8 NPT Male, 250°F Maximum Temperature	Barbed fitting for 3/32" transducer tubing (pack of 10)	McMaster-Carr	5121K361	4	$5.31
	Super-Flow Barbed Fitting for Food and Beverage Plastic Adapter for 1/4" Tube ID x 3/4 NPT Male	Barbed fittings for 1/4" nitrogen/rebalance tubing (pack of 10)	McMaster-Carr	2808K39	2	$17.36
Auxilliary connectors	Thick-Wall PVC Pipe Nipple for Water Fully Threaded, 3/4 NPT	Pipe nipples	McMaster-Carr	4882K14	10	$9.3
	Thick-Wall Polypropylene Pipe Fitting for Chemicals, Connector with Hex Body, 3/4 NPT Male	Pipe nipples with hex to replace pipe nipples	McMaster-Carr	46825K31	22	$12
	UV-Resistant Polypropylene Pipe Fitting for Chemicals, Tee Connector, 3/4 NPT Female	T connectors	McMaster-Carr	46885K153	11	$59.18
	Thick-Wall Polypropylene Pipe Fitting for Chemicals Bushing Adapter, 3/4 NPT Male x 1/8 NPT Female	Bushing between tee and transducer	McMaster-Carr	46885K254	4	$11.32
	PVC On/Off Valve for Drinking Water PTFE/HDPE Seat, 3/4 NPT Female, White	Isolation Valve	McMaster-Carr	4876K12	10	$95.6
Tubing	High-Flex Rubber Tubing for Chemicals 1/2" ID, 3/4" OD, 25 ft	Tank Tubing	McMaster-Carr	51225K43	2	$105.5
	High-Flex Rubber Tubing for Chemicals 3/4" ID, 1" OD, 5 ft	Stack tubing	McMaster-Carr	51225K47	1	$14.6
	PVC Tubing for Chemicals, 3/32" ID, 5/32" OD, 25 ft	Tubing to connect tee to transducer	McMaster-Carr	5231K134	1	$5.25
	High-Flex Rubber Tubing for Chemicals, 1/4" ID, 1/2" OD, 25 ft	Tubing for nitrogen cylinder	McMaster-Carr	51225K29	1	$31.50
	High-Flex Rubber Tubing for Chemicals, 1/4" ID, 1/2" OD, 10 ft	Tubing for electrolyte rebalancing	McMaster-Carr	51225K29	1	$12.60
Tube clamps	Noncontact Flow-Adjustment Valve Nickel-Plated Brass, for 3/32" to 3/4" Tube OD	Clamp-like (isolation) valves	McMaster-Carr	5330K23	8	$59.36
	Constant-Tension Spring-Band Clamps for 3/4" OD Hose and Tube	Spring clamps for 3/4" OD tubing	McMaster-Carr	7329K13	3	$18.30
	Constant-Tension Spring Clamps 17-7 PH Stainless Steel, for 1" OD Firm Hose and Tube	Spring clamps for 1" OD tubing	McMaster-Carr	5324K91	1	$8.01
	Constant-Tension Spring Clamps 17-7 PH Stainless Steel, for 1/2" OD Firm Hose and Tube	Spring clamps for 1/2" OD tubing (pack of 50)	McMaster-Carr	5324K42	1	$12.36
	Tight-Seal Bolt Clamps for Soft Hose and Tube, Galvanized Steel with Zinc-Plated Steel Screw, 31/64" to 37/64" ID	Clamps for 1/4" ID tubing (nitrogen)	McMaster-Carr	53175K87	1	$12.46
	Noncontact Flow-Adjustment Valve, Nickel-Plated Brass, for 3/32" to 3/4" Tube OD	Tube flow control clamps	McMaster-Carr	5330K23	4	$29.68

Table A.3: VRFB System costs Part 2

Other Equipment						
Auxilliary	Reusable Nylon Cable Tie Push Release, Standard, 12” Long, Off-White	Zip ties for keeping tubing fixed to frame	McMaster-Carr	7134K111	1	$9.38
	Thread Sealant Tape, 0.0032” Thick, 1/4” Wide, 14 Yard Long	1/4” teflon tape	McMaster-Carr	6802K11	1	$2.24
	Thread Sealant Tape, 0.0032” Thick, 1/2” Wide, 14 Yard Long	1/2” teflon tape	McMaster-Carr	6802K12	2	$5.24
	Dispensing Gun for Two-Part Cartridge	Dispensing Gun (startup cylinder adhesive)	McMaster-Carr	74695A71	1	$23.76
	2 oz. Plastic Funnel with Vapor-Lock Resistant Ridges	Funnel for transferring electrolyte	McMaster-Carr	4383T1	1	$1.08
	Plastic Drum Pump for Thick Liquids, 5.0 oz./Stroke, for 5 to 15 Gallon Container	Hand Pump	McMaster-Carr	4938K11	1	$44.89
	Plastic Drum Pump for Thin Liquids 22.0 oz./Stroke, Tube Discharge	Hand pump	McMaster-Carr	2578K35	1	$47.61
	Brass, Dual Stage Regulator, 0-120 psi Outlet Pressure	Pressure regulator for nitrogen gas cylinder	Praxair	PRS20123331-580	1	$423.53
	Plastic Pan, 18” Wide, 26” Long, 1” High	Drip tray for stack and tanks	McMaster-Carr	9989T56	3	$58.98
	Polystyrene Plastic Pan 19” Long, 13-3/4” Wide, 4-3/8” High	Pan for holding start-up tanks and pumps	McMaster-Carr	4515T23	2	$39.38
	Collapsible Spill-Control Tray for Six 55-Gallon Drums	Spill control tray	McMaster-Carr	2093T27	1	$320
Safety	32 oz. Saline Refill Bottle	Liquid for emergency eye wash station	Uline Canada Corporation	S-10492	2	$21.05
	Chemical- and Acid-Resistant Gloves, 20 Mil Thick, size Large	6 Reusable gloves	McMaster-Carr	5306T34	2	$9.78
	Disposable Nitrile Gloves, Chemical Resistant, Powdered, Smooth, 4 Mil Thick, Size large	100 Disposable gloves	McMaster-Carr	52555T3	1	$15.9
	Continuous Paper Towel Rolls, 8” Wide x 5-1/4” Diameter x 350 Feet Long	Paper towels 12 pack	McMaster-Carr	30005K3	2	$96.44
Water/ Chemicals	Deionized Water-100%, 5 Gallon Pail	DI water	McMaster-Carr	3190K741	10 Gallons	$46.46
	WTR DI ASTM II LABCHEM 20LT	Deionized water	Fisher Scientific	LC267505	2	$54
	Vanadium Electrolyte Solution –¿ 1.6 M V(3.5+), 2 M H2SO4, 0.05 M H3PO4)	Electrolyte	Oxkem	VOS16	100 L	$2955.79
	NITROGEN 99.998% T	Nitrogen gas	Praxair	NI 4.8-T	1	$38.90
Electronics						
Sensors	Flow Transmitter for Water Polypropylene Plastic Body, 1/4 NPT Female, 0.1 to 5 gpm	Flowmeter	McMaster-Carr	9687K11	2	$289.2
	PRESSURE SENSOR, 15 PSIG, ANALOG	Pressure transducer for stack	Digi-key	BPS140-HG015P-1SGCT-ND	4	$232.69
	AC/DC CONVERTER 5V 15W	Power supply for pressure transducers and flow transmitter	Digi-key	1866-4133-ND	1	$10.44
Pump	MAG DRIVE PUMP-INTG 9-24VBLDC EPDM	Pump	AOP Technologies	INTG3-572	2	$524
	AC/DC CONVERTER 24V 211W	Power supply for pumps	Digi-key	1866-3332-ND	1	$32.33
	CORD 18AWG NEMA5-15P - CBL 9.84’	Power supply cord	Digi-key	839-1263-ND	1	$6.70
	High-Starting-Current Rocker Switch Washdown, 1 Circuit	Rocker switch for pump power	McMaster-Carr	7194K45	2	$18.22
	Cover for 1.13” High x 0.88” Wide Maximum Cutout Rocker Switch	Cover for rocker switch	McMaster-Carr	1730N12	2	$5.5
	Inline Fuse Fast-Acting, 5A	Inline fuse for pump circuit	McMaster-Carr	73405K316	4	$11.52
	Holder for 1 Inline Fuse	Inline fuse holder	McMaster-Carr	73405K11	2	$5.26
Auxiliary	Patch Cord, Stackable Banana Plug x Stackable Banana Plug, Red, 60”	Cable for load bank	McMaster-Carr	6927K41	2	$13.7
	CONN SPLICE 16-22 AWG CRIMP	Crimp wire connectors	Digi-key	A0997-ND	100	$15.77
	CONN SPADE TERM 16-22AWG #4 RED	Spade terminals	Digi-key	A121038-ND	50	$10.75
	CABLE 3COND 22AWG GRAY 100’	Wiring	Digi-key	CE1003SG-100-ND	1	$27.18
	Ceramic-Tube Fuse, Fast-Acting, 25A, 250V AC/125V DC	Fuses for stack	McMaster-Carr	71385K635	4	$36.72